Journal of Materials Research and Technology 38 (2025) 5389–5408

Contents lists available at ScienceDirect

Journal of Materials Research and Technology

journal homepage: www.elsevier.com/locate/jmrt

Grain size effects in $BaTi_{0.90}Hf_{0.10}O_3$ ceramics with phase coexistence: the influence of nanostructuring and of the internal stress on the functional properties

Elena Mirabela Soare [a,b], Cătălina-Andreea Stanciu [b,c], Roxana Elena Pătru [d], Vasile-Adrian Surdu [e], Leontin Pădurariu [f], Nadejda Horchidan [g], Adrian-Ionuţ Nicoară [b], Lucian Trupină [d], Bogdan Ştefan Vasile [b], Roxana Doina Truşcă [b], Liliana Mitoşeriu [f], Adelina-Carmen Ianculescu [b,*]

[a] Institute of Physical Chemistry "Ilie Murgulescu", Romanian Academy, 202 Splaiul Independenței, Bucharest, 060021, Romania
[b] National University of Science and Technology Politehnica Bucharest, Faculty of Chemical Engineering and Biotechnologies, Department Science & Engineering of Oxide Materials and Nanomaterials, 1-7 Gh. Polizu, Bucharest, 011061, Romania
[c] National Institute for Lasers, Plasma and Radiation Physics, Atomiştilor 409, Măgurele, 077125, Romania
[d] National Institute for Materials Physics, Atomiştilor 405A, Măgurele, 077125, Romania
[e] Transilvania University of Braşov, Faculty of Materials Science and Engineering, Department of Materials Science, Bv. Eroilor 29, 500036, Brasov, Romania
[f] Alexandru Ioan Cuza University, Faculty of Physics, Bv. Carol I 11, Iaşi, 700506, Romania
[g] Alexandru Ioan Cuza University, Inst. of Inderdisciplinary Research, Science Res. Dept., RAMTECH Centre, Bv. Carol I 11, Iaşi, 700506, Romania

ARTICLE INFO

Keywords:
$BaTi_{0.90}Hf_{0.10}O_3$ ceramics
Landau-based calculations
Phase superposition
Spark plasma sintering
Energy storage properties

ABSTRACT

The present study is focused on describing the influence of the sintering method (fast field-assisted Spark Plasma Sintering *vs.* conventional sintering) on the functional properties of $BaTi_{0.90}Hf_{0.10}O_3$ ceramics with polymorph superposition around room temperature. Dense ceramics, derived from nanopowders synthesized *via* Pechini method, with grain size downscaled from 3.7 to 0.07 μm were prepared using different sintering strategies. XRD data at room temperature revealed the presence of mixtures of dissimilar structural modifications either for the starting nanopowder, as well as for the related ceramics. The Landau-based calculations indicated that different amounts of polymorphs are stable in these ceramics, by considering the grain size reduction and the strain-stress fields produced by the fast sintering method, thus confirming the experimental results of the structural and Raman analyses. By decreasing the average grain size from micro-to nanoscale, a slight decrease of the Curie temperature, accompanied by the increase of the diffuseness of the ferroelectric-to-paraelectric phase transition and the decrease of both the permittivity maxima and the dielectric losses was detected. Both the dielectric response and the ferroelectric $P(E)$ loops indicated a ferroelectric-relaxor crossover as the grain size decreased in the nanometre range. The beneficial effect of the nanostructuring on the energy storage efficiency was also revealed.

1. Introduction

In recent years, intensive research and development efforts have been dedicated to lead-free ferroelectric materials due to their potential use in multi-layer ceramic capacitors (MLCC) for high-power applications, non-volatile memories, piezoelectric actuators, pyroelectric IR sensors, thermistors, energy storage and tunable high-frequency devices, as phase shifters, filters, antennas, etc. [1–6]. For each kind of purpose, specific requirements are desired. For example, energy storage applications demand for materials with high permittivity, low losses, moderate polarization and high breakdown field [7,8], while microwave devices require dielectrics with high electric-field tunability ($n = \varepsilon(E)/\varepsilon(0) \geq 1.5$), moderate permittivity below 1000 and low dielectric losses (below 3 %) [9,10]. All of these requests can occasionally be incompatible with one another, and there is a strong interest to customize the electrical characteristics by discovering new materials,

* Corresponding author.
E-mail addresses: a_ianculescu@yahoo.com, adelina.ianculescu@upb.ro (A.-C. Ianculescu).

https://doi.org/10.1016/j.jmrt.2025.08.195
Received 6 July 2025; Received in revised form 21 August 2025; Accepted 22 August 2025
Available online 27 August 2025

material combinations, or processing parameters to provide nano/-microstructural control.

Among the environmentally friendly lead-free ferroelectric perovskites, the model ferroelectric system $BaTiO_3$ has attracted considerable attention as a key electroceramic material [11,12]. $BaTiO_3$ (BT) presents four structural polymorphs: (*i*) rhombohedral (R, *R*3*m*) below −90 °C, (*ii*) orthorhombic (O, *Amm*2) in the range (−90, 5)°C, (*iii*) tetragonal (T, *P*4*mm*) between (5, 120)°C and (*iv*) cubic (C, $Pm\ \bar{3}\ m$) above the Curie temperature T_C = 120 °C [2]. Its spontaneous polarization can be switched under the application of the electric field between energetically equivalent orientations (6, 12 and 8 for the T, O and R polymorphs, respectively), with a hysteretic polarization-field variation. Since the structural transitions are accompanied by enhancements of the functional responses (*i.e.* high material constants), a way of engineering $BaTiO_3$-based materials towards superior properties is to be used in the range of their structural transformations [13–16], although this may pose limitations concerning the thermal stability of devices. The main disadvantages for using pure $BaTiO_3$ (BT) in applications are related to the hysteretic $P(E)$ and $\varepsilon(E)$ dependences, sharp temperature variation of the functional properties at the structural transformations and high losses caused by domain walls relaxations [17]. To reduce such drawbacks while preserving high permittivity, polarization and/or tunability, according to the applications needs, lead-free homovalent $BaTiO_3$ solid solutions have been proposed, following the idea to find a compromise between such contrasting trends [18]. Among them, *B*-site homovalently substituted solid solutions as $Ba(Ti,Zr)O_3$ (BTZ) [18–22], $Ba(Ti,Sn)O_3$ (BTS) [23–29], $Ba(Ti,Ce)O_3$ (BTC) [30] or $Ba(Ti,Hf)O_3$ (BTH) [31–41] can provide high tunability and reduced hysteresis looparea, high electrocaloric effect [42], or increased permittivity giving rise to high energy-storage density (W_{rec}), and superior storage efficiency (η) [43–46]. For all the $BaTi_{1-x}M_xO_3$(M^{4+} = Zr^{4+}, Sn^{4+}, Ce^{4+}, Hf^{4+}) solid solutions, a ferroelectric-to-relaxor crossover with modification from a long-range ferroelectric order to a nanopolar short-range order takes place, when increasing the substitution degree *x*. Additionally, the Curie temperature T_C decreases as the substitution degree *x* increases, while the temperatures associated with the other structural transformations increase until they meet at the phase convergence point, resulting in the "pinched" transition within the compositional range of about 0.09–0.15, depending on both the solute nature and ceramic grain size induced by the processing conditions [22–24,27,28,47–50].

Despite their high chemical stability and promising dielectric performances, $Ba(Ti,Hf)O_3$ (BTH) compositions have been much less studied than other BT-based solid solutions and only a few reports concerning coarse-grained ceramics derived from conventionally prepared solid-state powders [31–40,51,52] are found in the literature. No systematic study regarding the influence of microstructural features on the crystal structure and functional properties in multiscale-structured $Ba(Ti,Hf)O_3$ ceramics was provided so far.

As mentioned, in the BT-based solid solutions, the temperature ranges for the polymorph transformation are tuned by the substitution degree, thus providing a strategy for maximizing dielectric, ferroelectric, piezoelectric and energy storage performance at specific compositions around the polymorphic phase boundaries (PPBs), where multiple phases with different symmetries may coexist [13–15,41,53]. In spite of the similar general trends concerning the temperature-dependence of the phase composition in all the $BaTi_{1-x}M_xO_3$ solid solutions with any homovalent M^{4+} substitution, the literature experimental data indicate different values for the critical concentrations of the "pinched" transition, for the relative amounts of polymorphs at a given solute concentration and for the diverse electrical properties, even for the same composition of the mixed crystals [50,53]. This effect can be explained by considering that in such a multifunctional system with phase coexistence, the equilibrium between crystallographic symmetries separated by small energy barriers can be easily disturbed by factors like local electric and strain-stress fields, which can differ according to the nano/microstructural characteristics of each composition, which in turn, are determined by the starting powders characteristics and ceramic processing parameters. In order to illustrate this effect, at least at a qualitative level, a Landau-Devonshire theory-based model is proposed in the following.

2. Theory: Landau-Devonshire theory-based calculations

The role of homovalent substitution on the phase stability and temperature evolution of polymorph phases in $Ba(Ti,M^{4+})O_3$ (M^{4+} = Zr^{4+}, Sn^{4+}, etc.) solid solution can be described in a qualitative approximation by using Landau-Devonshire theory calculations, as proposed by Bell & Cross, initially for single-crystals [54–56] and further applied for polycrystalline ceramics [57,58]. A recent novel method was developed to explain the enhanced properties of $BaTi_{1-x}Sn_xO_3$ ceramics with phase coexistence [59]. In this approach, the Landau free energy was used at local scale to describe ceramic single grains and then, statistical averaging is performed over all the grains orientations found in different crystalline states, in order to retrieve the average ceramic properties.

The simulations are based on a sixth order free energy *G* expansion on polarization components P_i originally proposed in Ref. [56]:

$$\begin{aligned} G_{stress-free} = {} & \alpha_1\left(P_1^2+P_2^2+P_3^2\right)+\alpha_{11}\left(P_1^4+P_2^4+P_3^4\right) \\ & +\alpha_{12}\left(P_1^2P_2^2+P_1^2P_3^2+P_2^2P_3^2\right)++\alpha_{111}\left(P_1^6+P_2^6+P_3^6\right) \\ & +\alpha_{112}\left[P_1^2\left(P_2^4+P_3^4\right)+P_2^2\left(P_1^4+P_3^4\right)+P_3^2\left(P_1^4+P_2^4\right)\right]+\alpha_{123}P_1^2P_2^2P_3^2 \end{aligned} \quad (1)$$

where P_1, P_2, P_3, and E_1, E_2, E_3 are the components of the polarization vector on [100], [010], and [001] axis of a single-crystalline ceramic grain, while the $\alpha_1, \alpha_{11}, \alpha_{111}, \alpha_{12}, \alpha_{112}, \alpha_{123}$ are parameters dependent on temperature and on the substitution degree with M^{4+} onto Ti^{4+} positions in the BT solid solution and are considered a reference for the coarse stress-free ceramic. To derive the phase polymorphs at a given temperature, the stable minima of the Gibbs free energy for different values of the polarization components (P_1, P_2, P_3) are determined by simulations. The minimum free energy corresponds to the following crystalline polymorphs: (*i*) $P_1 = P_2 = P_3 \neq 0$ (R), (*ii*) $P_1 = P_2 \neq 0, P_3 = 0$ and the analogous cases (O), (*iii*) $P_1 \neq 0, P_2 = P_3 = 0$ and the analogous cases (T), and (*iv*) $P_1 = P_2 = P_3 = 0$ (C). The employed parameters are derived from the ones corresponding to the pure $BaTiO_3$ proposed by Bell & Cross [54,55] by considering the condition of all the four polymorph coexistence at the triple point for *x* =12 %, similarly as proposed in Ref. [59]. More details concerning numerical values of the α parameters, the minimization/relaxation algorithms for describing the state of a single grain, as well as the method to statistically derive the amounts of the phases at various temperatures and compositions are presented in ref. [59]

Fig. 1 shows representations of the room temperature free energy for different orientations of polarizations with respect to P_1, P_2, P_3 axes for variable substitution degree level: *x* = 0, 4 %, 7 % and 10 % in the $BaM_xTi_{1-x}O_3$ solid solutions. The 3D representations of the free energy from Fig. 1(a)–(d) indicate the stable polymorph states by the free energy minima (indicated in blue colour), as following: for *x* = 0, T state is dominant, but also O state is stable, for *x* = 4 % O is dominant, but also T is stable, while for *x* = 10 %, the minimum free energy corresponds to the R polymorph, but the energy barrier between R and O states is very small.

The computed crystalline phase amounts corresponding to the four compositions as a function of temperature presented in Fig. 1(e)–(h) are very interesting, because they indicate temperature ranges where phases may coexist. Among them, the composition x = 10 % is one of the most interesting, because it presents around room temperature, in the range of (10 − 40)°C, all the possible polymorphs, with predominant R and O phases, for which 20 possible polarization orientations are allowed (12 in O state and 8 in R state). Due to this, an easy polarization rotation-like

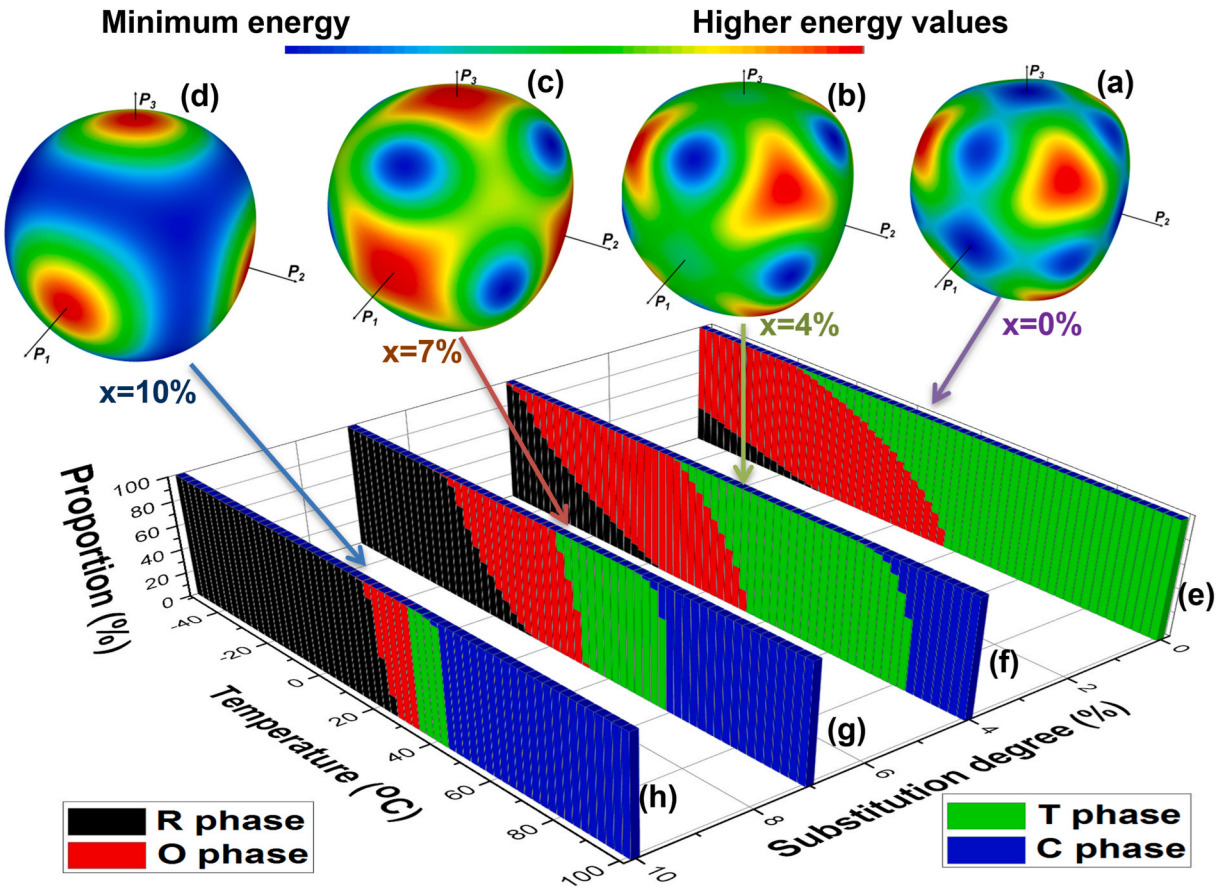

Fig. 1. Representation of surfaces corresponding to the free energy minimum positions for different orientations (components) of polarization vectors for a stress-free coarse ceramic with a few substitution levels: (a) x = 0 %, (b) 4 %, (c) 7 % and (d) 10 % in $BaTi_{1-x}M_xO_3$ solid solutions at room temperature (the free energy value on these surfaces is represented in colour scale); (e)–(h) the weight of the polymorph phases (R, O, T and C) *vs.* temperature, calculated for the corresponding compositions.

switching mechanism between multiple states under the applied field is likely and therefore, enhanced functional responses may be expected for this composition. The mechanism of enhancing properties by the existence of easy paths for polarization rotation in a flattened free energy profile generated by phase coexistence was proposed by Damjanovic [60] and it was firstly demonstrated experimentally for $BaTi_{1-x}Sn_xO_3$ ceramics in Ref. [57].

Further, the phase equilibrium can be disturbed in BT-based polycrystalline ceramics not only by composition, but for a specific composition, by variable processing methods giving rise to modifications of grain size, local variations of the internal strain-stress fields, porosity or different types of grain boundaries.

In previous works, modifications of the polymorph amounts in BT ceramics have been found to be produced by the grain size reduction at nanoscale [61], or by variations of local strains induced by porosity [62]. To describe the effect of the grain size (*GS*) reduction for a fixed composition (x = 10 %), the parameters α_1 and α_{12} are modified, as following:

$$\alpha_1 = \alpha_{10}(t - t_C) + K_1 / GS, \tag{2}$$

where α_{10} and K_1 are constants, t_C is the Curie temperature, and:

$$\alpha_{12} = \alpha_{12}' + K_2/GS, \tag{3}$$

where α_{12}' and K_2 are constants. The numerical values of the K_1 and K_2 were considered identical with the ones for $BaTiO_3$ reported in Ref. [61].

In addition, the role of local stress was added to the free energy accordingly to the following equation:

$$G = G_{stress-free} - Q_{11}\left(\sigma_1 P_1^2 + \sigma_2 P_2^2 + \sigma_3 P_3^2\right) - Q_{12}\left(\sigma_1\left(P_2^2 + P_3^2\right) + \sigma_2\left(P_1^2 + P_3^2\right) + \sigma_3\left(P_1^2 + + P_2^2\right)\right) - Q_{44}\left(\sigma_4 P_1 P_2 + \sigma_5 P_1 P_3 + \sigma_6 P_2 P_3\right), \tag{4}$$

where Q_{11}, Q_{12} and Q_{44} are electrostrictive coefficients, σ_1, σ_2 and σ_3 are tensile/compressive stresses, and σ_4, σ_5 and σ_6 are the shear stresses. The numerical values of the new parameters presented in Eq. (4) are those reported in Ref. [62].

Starting from the free energy corresponding to the stress-free coarse ceramic with $x = 10$ % substitution, such additional terms (eq. (4)) have been added in the free energy expansion and the new free energy minima have been determined. The results of such calculations presented in Fig. 2 illustrate the effect of the two main parameters on the free energy diagram and on the phase composition: (*i*) the randomly distributed stress effects (considered for example along one direction P_1) and additionally, (*ii*) the contribution of grain size reduction towards nanoscale. The obtained computed results indicate a general trend at a qualitative level, irrespective on the nature of M^{4+} substituent onto the Ti^{4+} sites of $BaTiO_3$ ceramics and represent a guide concerning the composition selection and parameters possible to be used to tailor the phase superposition range in such polycrystalline solid solutions. The local stresses (stretching, elongation and shear) randomly applied to different directions favour at room temperature a low energy barrier between O and T states in a predominant T structure. If additional to the stresses, *GS* reduction towards nanoscale is considered by including in the free energy terms from eqs. (2) and (3), an overlapping of R and C polymorphs is induced. Therefore, in compositions with phase

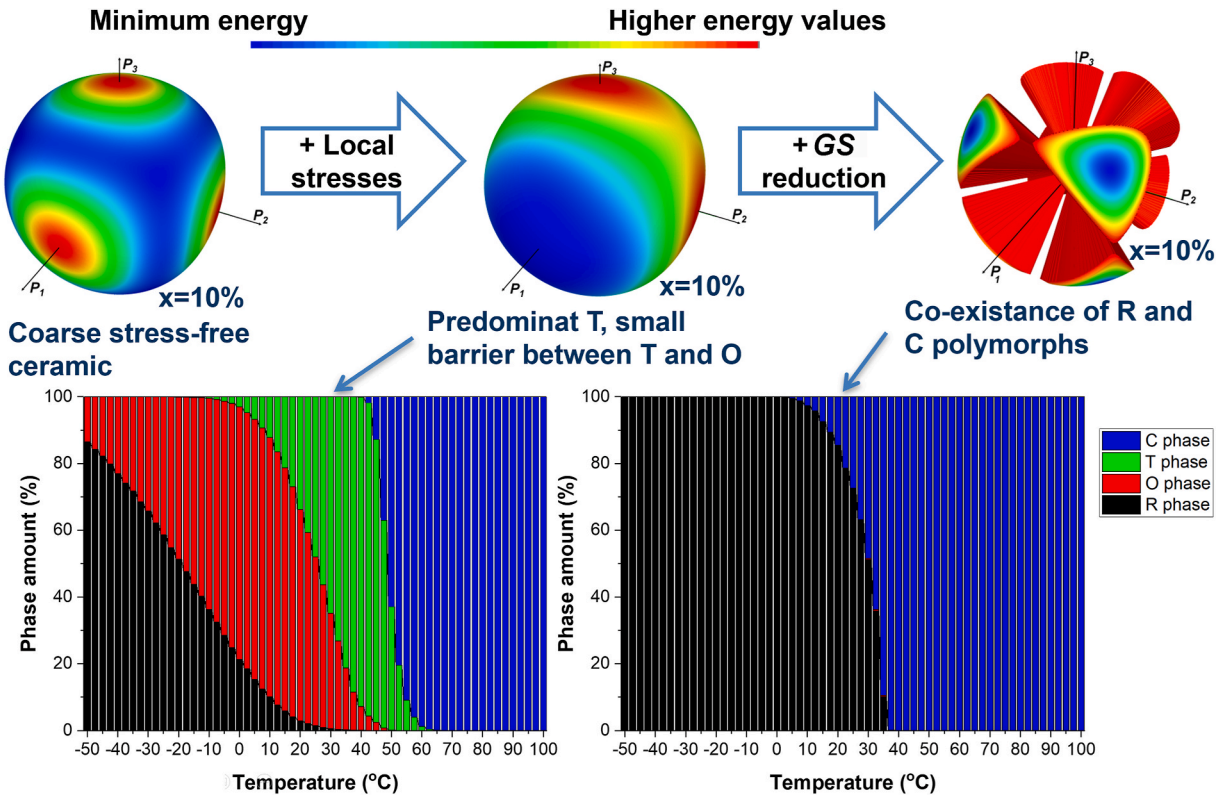

Fig. 2. Diagram presenting the effect of local stress and grain size reduction on the free energy and on the phase composition *vs.* temperature dependences, as computed by Landau theory-based simulations of $Ba(M_xTi_{1-x})O_3$ ceramics.

coexistence, the polymorph composition can be modified by processing parameters giving rise to internal strain-stress fields and by downscaling the ceramic grain size, thus inducing modifications of the functional properties.

According to the theoretical predictions and by considering the scarce literature data concerning the Hf-doped BT ceramic system among the $Ba(Ti_{1-x}M_x)O_3$ solid solutions, the composition $BaTi_{0.90}Hf_{0.10}O_3$ obtained from nanopowders synthesized by the modified Pechini method [63] was selected in the present study for investigation. The influence of the processing methods (conventional sintering to produce coarse ceramics *vs.* spark-plasma sintering providing nanostructuring) on the phase composition, phase transitions and on the functional properties (dielectric, ferroelectric behaviour and energy storage performance) is reported.

3. Experimental

3.1. Samples preparation

Previous works on SP-sintered BT ceramics revealed that the grain growth rate during this fast sintering is very sensitive to the type of the wet-chemical method used for the powder preparation [64,65]. Thus, for certain wet-chemical techniques, as the acetate variant of the sol-gel method or the sol-precipitation route, despite the low size of the starting particles, their growth is very fast with temperature increase during the SPS process. Taking into account the results reported by Li et al. [64], BTH nanopowder synthesized by the modified Pechini method [63] was considered the most appropriate to be consolidated by SPS, in order to obtain dense, nanocrystalline ceramics.

Three types of ceramics have been produced by using the same nanopowder: (*i*) conventionally sintered in air at 1400°C/4 h, denoted as *BTH_CS* and SP-sintered under a pressure of 50 MPa pressure at: (*ii*) 1200 °C/2 min (*BTH_SPS1*), and (*iii*) 1050 °C/2 min (*BTH_SPS2*). All the details concerning the synthesis of nanopowders and concerning the ceramic consolidation are presented in the Annex 1, Supplementary Material (Fig. S1).

3.2. Characterization methods

To assess the purity of the perovskite phase in the $BaTi_{0.90}Hf_{0.10}O_3$ powders and related ceramics X-ray diffraction (XRD) investigations were performed at room temperature (RT) with an Empyrean diffractometer (PANalytical, Almelo, The Netherlands) with Ni-filtered CuKα radiation ($\lambda = 1.541874$ Å), operating at 45 kV and 40 mA in $\theta - \theta$ geometry. A scan step increment of 0.026° and a counting time per step of 255 s in the 2θ range of (20–80)° were chosen for the XRD measurements. The recorded XRD patterns were processed with the HighScorePlus3.0.e software. For the phase identification the ICDD PDF-4+ 2024 database was used. The lattice parameters, mean crystallite size (<*D*>) and internal micro-strains (<*S*>) were determined by Rietveld refinement with the HighScore Plus 3.0.e software, using a polynomial function for background approximation, a pseudo-Voigt function for peak profile, and a Caglioti function for peak width. The lattice parameters were calculated by applying the Least Squares Procedure (LSP) method, using the linear multiple regressions for several diffraction lines, depending on the symmetry of the unit cell.

A FEI QUANTA INSPECT F50 scanning electron microscope with field emission gun (FEI, Hillsboro, OR, US) operating at 30 kV, as well as a TITAN THEMIS ultra-high resolution electron microscope (Thermo Fisher Scientific, Waltham, MA, USA) operating at 300 kV equipped with a STEM/HAADF detector and an energy-dispersive (EDS) X-ray microprobe were used to investigate the particle morphology and to check the elemental composition. TEM analysis is also coupled with selected area electron diffraction (SAED), which provides information regarding the crystallinity and the local structure of the BTH nanoparticles. The same FE-SEM equipment was also used to analyze the

microstructure of the related BTH ceramics. Both the average particle size <*d*> in the starting nanopowder and the average grain size, <*GS*> for the ceramics were estimated from the particle/grain size distributions, which were determined using the OriginPro 9.0 software (OriginLab, Northampton, MA, USA) by taking into account size measurements on ~100 particles/grains performed by means of the software of the electron microscopes (ImageJ 1.50b, National Institutes of Health and the Laboratory for Optical and Computational Instrumentation, Madison, WI, USA, in the case of the scanning electron microscope and Digital Micrograph 1.8.0, Gatan, Sarasota, FL, USA, in the case of the transmission electron microscope). The relative density values of the sintered BTH ceramic samples were calculated as ratio between the apparent density measured by the Archimedes' method and the crystallographic (theoretical) density determined from the XRD data.

The ferroelectric local switching and domains size were investigated/estimated using vertical piezoresponse force microscopy (V-PFM). V-PFM measurements were performed using a MFP-3D SA atomic force microscope (Asylum Research, Oxford Instruments, Santa Barbara, United States) operating in Dual AC Resonance Tracking (DART) mode. This technique allows for enhanced sensitivity in the detection of piezoelectric signals by continuously tracking the contact resonance of the cantilever. A solid conductive platinum-coated cantilever (Rocky Mountain Nanotechnology, model RMN-25PT300B) with a nominal spring constant of 18 N/m was employed for all measurements. The conductive tip enables simultaneous topographical and electromechanical imaging by applying an AC voltage and measuring the resulting mechanical response of the sample surface.

For electrical characterization, both faces of the sintered ceramic discs were polished and coated with silver paste to ensure good electrical contact and form parallel-plate electrodes. Impedance spectroscopy and phase shift measurements were performed in vacuum using a computer-controlled HIOKI 3536 LCR meter (Nagano, Japan). Data were acquired over a frequency span of 10^2–10^6 Hz, with a sinusoidal excitation of 1 V. The temperature-dependent measurements were conducted during controlled cooling from 470 K to 50 K at a rate of 1 K/min, with thermal stability maintained within ±0.03 K.

To measure the ferroelectric *P*(*E*) loops at room temperature, a Radiant Precision Multiferroic II Ferroelectric Test System (Radiant Technologies, INC., Albuquerque, New Mexico, USA) with a frequency of 1 Hz and double bipolar input as the electric signal was used. The applied field was increased until the electrical response became unstable, indicating the proximity of the ceramic sample's breakdown.

The local order in the BTH ceramics was investigated by Raman spectroscopy, using a LabRAM HR Evolution spectrometer (Horiba, Kyoto, Japan). The Raman spectra were obtained using the 514 nm line of an argon ion laser. The laser beam, with a power of 125 mW, was focused on spots of a few micrometers in size on the samples. Data were collected and analyzed for the non-polarized radiation scattered at 90°, with an acquisition time of 120 s during 3 runs recorded for each sample. To assess the type of the phase transitions, temperature dependence of Raman scattering was investigated by collecting spectra recorded between 148 and 473 K, with an increment of 25 K.

4. Results and discussions

4.1. Phase purity, crystal structure and morphology/microstructure

4.1.1. $BaTi_{0.90}Hf_{0.10}O_3$ nanopowder

The X-ray diffraction pattern recorded at room temperature showed a perovskite well crystallized single-phase composition for the as-synthesized $BaTi_{0.90}Hf_{0.10}O_3$ nanopowder (Fig. 3(a)). The Rietveld analysis indicated that actually the powdered sample consists of a mixture of two polymorphs: C (*Pm3 m*) and T (*P4mm*), with a prevalence of the C structure, as indicated in Table S1 of Annex 2, Supplementary Material and in the detail of the region corresponding to the diffraction angles $2\theta = 43.25$–$47.25°$ of the XRD pattern (Fig. 3(b)).

The structural features, *i.e.* the unit cell parameters and volume, theoretical density, mean crystallite size and internal micro-strains for each phase, together with the Rietveld fitting parameters are also listed in Table S1 of Annex 2, Supplementary Material.

The BTH powders were ultrasonically de-agglomerated, sieved and then, the particles morphology was investigated by FE-SEM and TEM analyses. The FE-SEM image of Fig. 4(a) indicates the presence of nano-sized particles with a certain agglomeration tendency, which only gives a rough estimation of particle size.

To clearly visualize the shape of the particles and rigorously determine their average size, TEM investigations were performed. The bright-field TEM image of Fig. 4(b) reveals equiaxed, evenly-sized particles, with unimodal size distribution, as indicated the histogram depicted as inset in the bottom-right corner of Fig. 4(b). The mean particle size <*d*> = (18.2 ± 4.7) nm estimated by statistical analysis is close to the

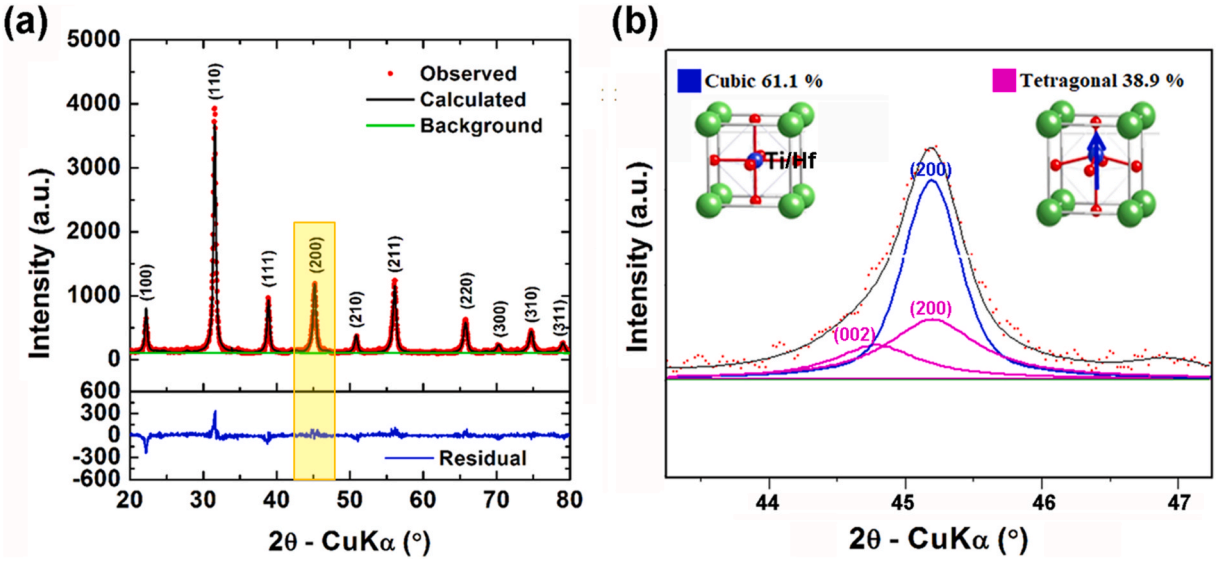

Fig. 3. (a) Room-temperature X-ray diffraction pattern for the $BaTi_{0.90}Hf_{0.10}O_3$ nanopowder prepared by the modified Pechini method and annealed at 900 °C for 2 h and (b) detail (the yellowish rectangle of Fig. 3(a)) of the region corresponding to the diffraction angles $2\theta = 43.25$–$47.25°$, showing the coexistence of a major cubic phase along with a minor tetragonal phase.

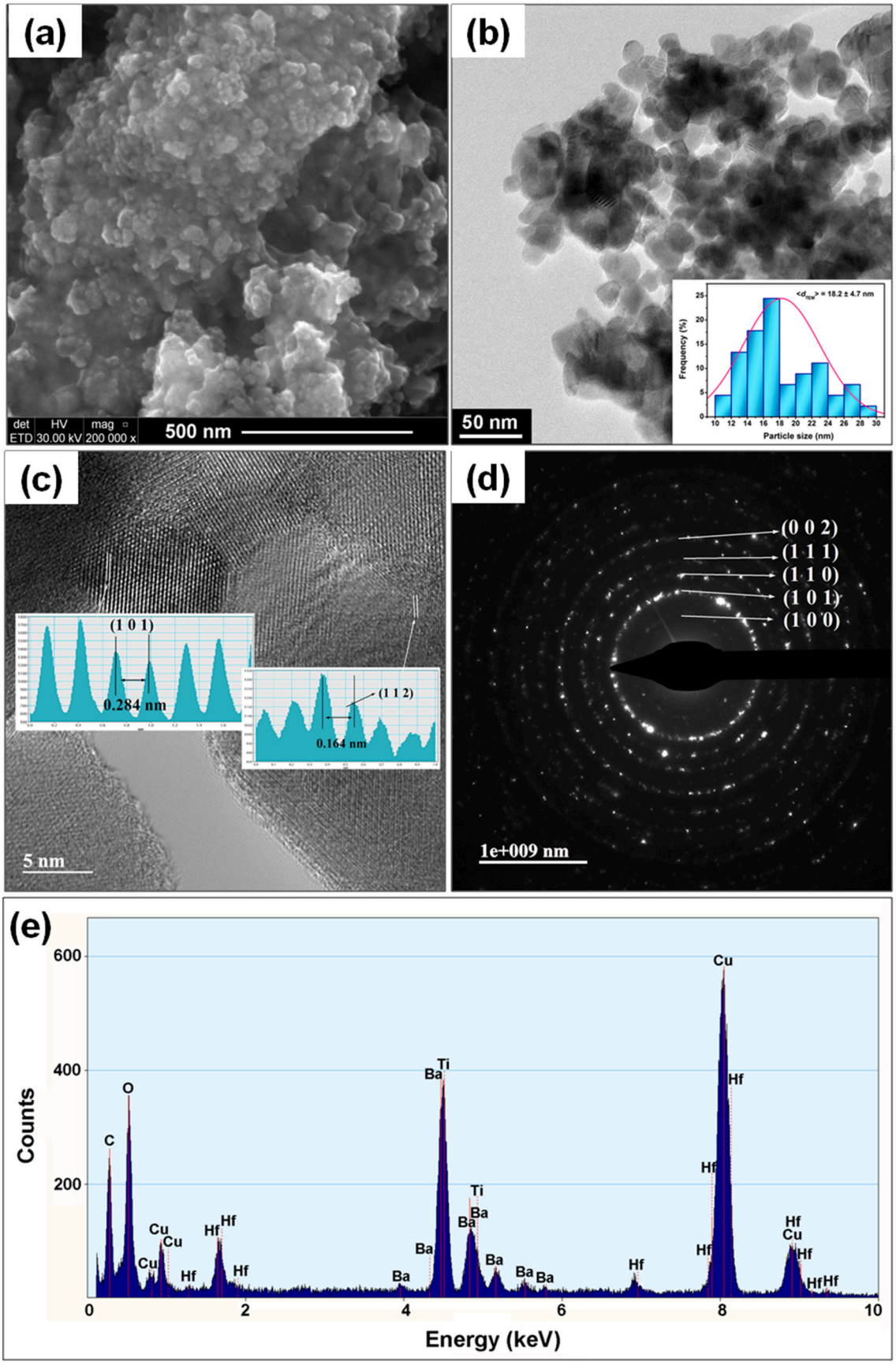

Fig. 4. (a) SEM image; (b) TEM image: inset in the bottom-right corner – histogram indicating the particle size distribution; (c) HRTEM image; (d) SAED pattern and (e) EDX spectrum of the $BaTi_{0.90}Hf_{0.10}O_3$ (*BTH*) powder.

mean crystallite size value ($<D \geq 20.0 \pm 3.1$) nm calculated from the XRD data (Table S1 of Annex 2, Supplementary Material), indicating that the BTH nanopowders consist of single-crystal particles, devoid of defects such as low-angle boundaries or dislocation networks, which usually affect the lattice order in single crystals. The high crystallinity degree is proven by the long-range ordered fringes showed by the HRTEM image of Fig. 4(c), as well as by the bright spots composing the concentric diffraction rings as indicates the SAED pattern of Fig. 4(d). The EDX spectrum recorded on the BTH powder shows exclusively peaks ascribed to the atomic species of the perovskite phase, *i.e.* Ba, Ti, Hf, and O (Fig. 4(e)), suggesting that no contamination took place during the powder synthesis process. It has to be mentioned that the presence of the C and Cu peaks is related to the holey carbon coated film Cu grid used for TEM investigation.

4.1.2. $BaTi_{0.90}Hf_{0.10}O_3$ ceramics

As the starting BTH nanopowder, the ceramic samples resulted after consolidation are free of residual Ba- or Ti-rich phases, consisting only of well-crystallized perovskite $BaTi_{0.90}Hf_{0.10}O_3$ solid solution, as shown in Fig. 5(a)–(d) and (g). The best fitting parameters of the Rietveld refinement (Table S2 of Annex 2, Supplementary Material) were obtained considering the coexistence of dissimilar polymorphs in all the three specimens under investigation, irrespective of the sintering technique used.

At room temperature, a mixture of a major (O) phase and a significantly lower amount of (R) phase was found for the ceramic sample (*BTH_CS*) obtained by conventional sintering, as indicates the deconvolution of the reflections located at ~45° and ~75° in the corresponding pattern (Fig. 5(b) and (c)), which also corresponds to the phase superposition determined for the stress-free coarse $BaTi_{0.90}Hf_{0.10}O_3$ ceramic by Landau free-energy calculations presented in Fig. 1. A similar mixture of polymorphs was also reported by Elorika et al. [52] for their $BaTi_{0.92}Hf_{0.08}O_3$ ceramic prepared by the solid-state-reaction method. For the BTH specimens consolidated by spark plasma sintering (SPS), the crystalline structure depends on the sintering temperature. Thus, a three-phase composition, consisting of a mixture of close proportions of orthorhombic (O) and tetragonal (T) modifications (O: 48.4 %, T: 43.2 %), together with a small amount of rhombohedral (R: 8.4 %) polymorphs, was detected for the (*BTH_SPS1*) sample sintered at higher temperature (Fig. 5(e) and (f)), while in the specimen SP-sintered at 1050°C (*BTH_SPS2*), a two-phased composition with R and C polymorphs was found (Fig. 5(h) and (i)). The modification of phase composition is related to the specific microstructural factors induced by the mechanisms involved in the SPS consolidation with respect to the conventional sintering, as it will be explained below.

The results displayed in Table S2 of Annex 2, Supplementary Material, show notable differences in the values of the mean crystallite size and internal micro-strains for dissimilar structural modifications. However, an inversely proportional relationship between the mean crystallite size and the mean value of the internal micro-strains, irrespective of the unit cell symmetry, can be noticed. For the samples consolidated by SPS, the unit cell symmetry of the major phase, *i.e.* the O in *BTH_SPS1* and R one in *BTH_SPS2*, could be influenced by particular microstructural features determined by the sintering temperature. It is expected that dissimilar microstructures will induce changes in the ferroelectric-paraelectric phase transition, accompanied by changes in the crystalline structure at room temperature. Further Raman investigations and dielectric measurements will clarify the role of the microstructural features, especially grain size, on the crystal structure of the BTH ceramics analyzed here.

The microstructure is determined by the sintering strategy used to consolidate the ceramic bodies (Fig. 6). All the specimens exhibit dense and homogeneous microstructures, with equiaxed grains, uniform as shape and size (Fig. 6(a)–(c), (e)).

The histograms depicted as insets in Fig. 6(a)–(c), (e) indicate unimodal grain size distributions, with average $<GS>$ values of 3.7 μm, 2.8 μm and 0.07 μm for the samples *BTH_SPS1*, *BTH_CS* and *BTH_SPS2*, respectively. Thereby, it was found that, no matter of the consolidation technique, coarse-grained samples, with almost similar average grain size in the micron range, resulted after sintering at higher temperatures (1400°C/4 h for CS and 1200°C/2 min for SPS (Fig. 6(a)–(c)), whereas a fine-grained specimen, with $<GS>$ downscaled in the nanometre range, was obtained after SPS at 1050°C/2 min (Fig. 6(e)).

Higher magnification FE-SEM images of Fig. 6(b)–(d), (f) show morphological details of the three types of samples investigated here. For the coarser ceramics, although the $<GS>$ is quite similar, some differences in the morphology of the grains, determined by the type of sintering, can be observed (Fig. 6(b) and (d)). Even if both specimens consist of polyhedral grains, the faceting of the grains is more pronounced and their shape is better defined in *BTH_SPS1* ceramic (Fig. 6 (d)), than in *BTH_CS* (Fig. 6(b)).

In *BTH_SPS1* the grains are tightly packed together, exhibiting well-defined edges, smooth faces, perfect triple junctions (Fig. 6(d)) and almost full densification. In *BTH_CS*, the more irregular shape of the grains and their rough faces seems to indicate as growth mechanism the coalescence of smaller grain into larger ones. This imperfect morphology determines the appearance of a small amount of inter-grain porosity, together with some small, isometric, intra-grain pores (Fig. 6(b)). For the nanocrystalline *BTH_SPS2* sample, despite the much lower $<GS>$ value relative to that one determined in *BTH_SPS1*, the specific features induced by the SPS processing, *i.e.* pronounced faceting, advanced densification and lack of porosity are maintained, as show the details presented in the high-magnification FE-SEM image of Fig. 6(f).

The observed phase composition and microstructural differences are related to the differences between the involved sintering methods. With respect to the conventional sintering, which takes place by a slow equilibrium densification process allowing the grain growth and equilibration of defects and of the local strain-stress fields, SPS provides a fast, non-equilibrium consolidation mechanism. It was demonstrated that internal strains and inhomogeneous stress fields are induced in ceramics by short-time SPS, in particular when using lower sintering temperatures [66–68], than those specific to the conventional sintering. Therefore, the BTH samples consolidated by SPS maintained a higher levels of internal strain-stress than that one consolidated by conventional sintering (Table S2 of Annex 2, Supplementary Material), even after the re-oxidation step. Additionally, their relative densities are higher: 99.7 % (*BTH_SPS1)* and 98.8 % (*BTH_SPS2*), with respect to 94 % for the ceramic (*BTH_CS*), which cause a higher level of the internal stress, also. The significant proportion of C modification found in the nanocrystalline *BTH_SPS2* ceramic could be explained in terms of a faster evolution toward the ferroelectric-paraelectric phase transition as result of *GS* reduction [69], together with the high strains exerted in the grain boundary regions induced by nanostructuring.

From the structural point of view, nano-sized grains can be likened to composite systems, consisting of ferroelectric cores with polar structure and non-ferroelectric layers, adjacent to the grain boundaries, exhibiting the so-called “pseudo-cubic structure” determined by complex stress-induced distortions, as recently reported for nanocrystalline $Ba_{0.8}Sr_{0.2}TiO_3$ ceramics [70]. For a nanocrystalline specimen, the lower *GS*, the higher is the density of both the grain-boundary regions and the related pseudo-cubic “dead layers”. Therefore, nanostructuring in *BTH_SPS2* specimen determines lower values of the average crystallite size, $<D>$ and higher internal micro-strains, $<S>$, as XRD data revealed. Such features have also been reported for other nanocrystalline $BaTiO_3$-based systems [70,71]. By considering terms related to the local stresses inside the ceramic body (randomly distributed shrinkage, stretching and shear stresses) in the Landau free energy of the coarse, stress-free ceramic system (assigned to the *BTH_CS* sample), a phase mixing consisting of T and O polymorphs was computed as stable (to be compared with major O, T polymorphs and small amounts of R states in the *BTH_SPS1* ceramic). When considering also the terms related to the *GS* reduction to the nanoscale, a similar phase composition (R and C co-existence) as in

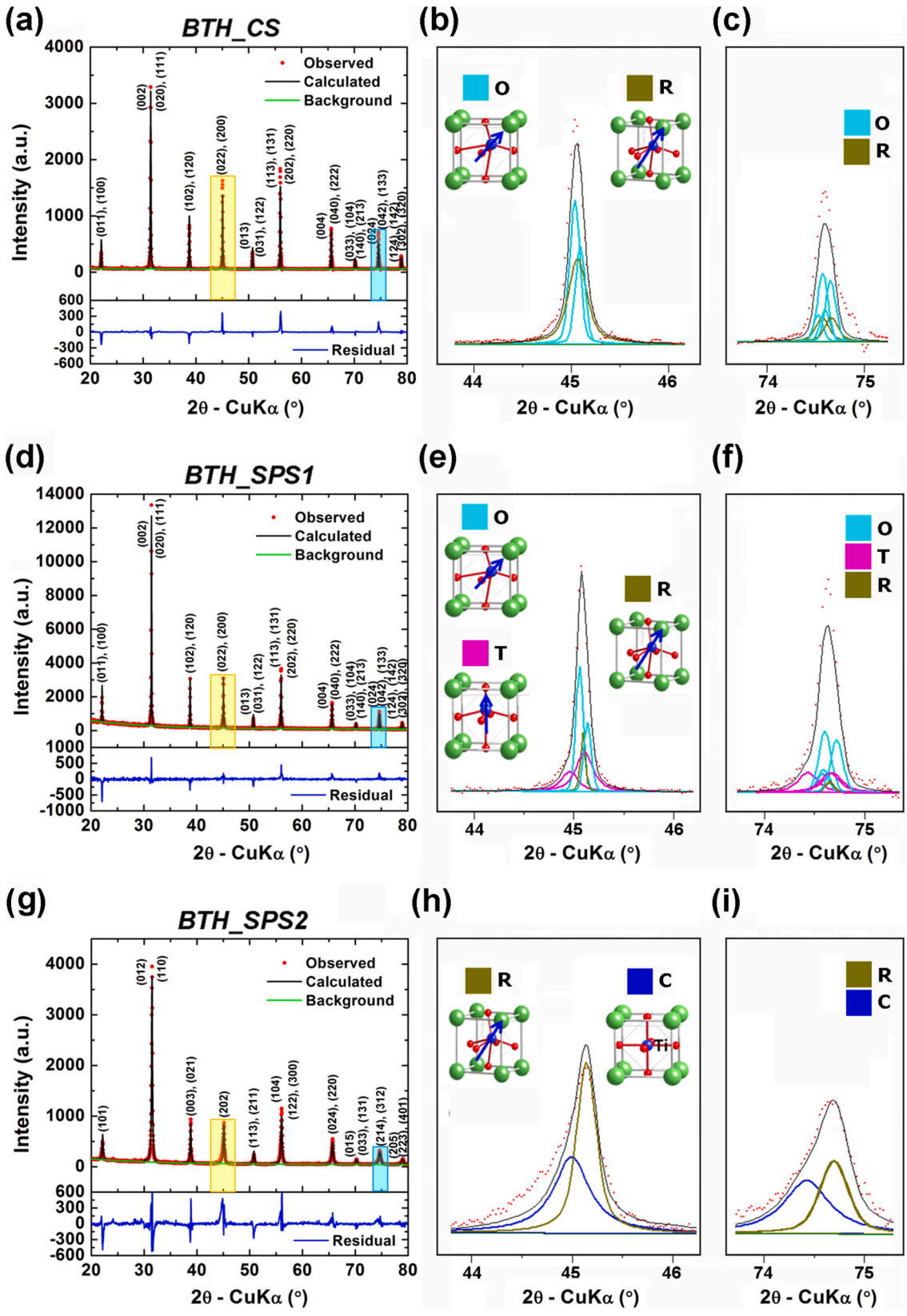

Fig. 5. (a)–(c) Room-temperature X-ray diffraction patterns for $BaTi_{0.90}Hf_{0.10}O_3$ ceramics consolidated by different strategies: (a) conventional sintering at 1400°C/4 h (*BTH_CS*), (d) spark plasma sintering at 1200°C/2 min (*BTH_SPS1*), (g) spark plasma sintering at 1050°C/2 min (*BTH_SPS2*); (b), (e), (h) details (the yellowish rectangles of Fig. 5(a)–(d), (g)) of the region corresponding to the diffraction angles $2\theta = (43.7–46.2)^\circ$ and (c), (f), (i) details (the light blue rectangles Fig. 5(a)–(d), (g)) of the region corresponding to the diffraction angles $2\theta = (73.7–75.5)^\circ$, showing the coexistence of BTH phases with different symmetries of the unit cell.

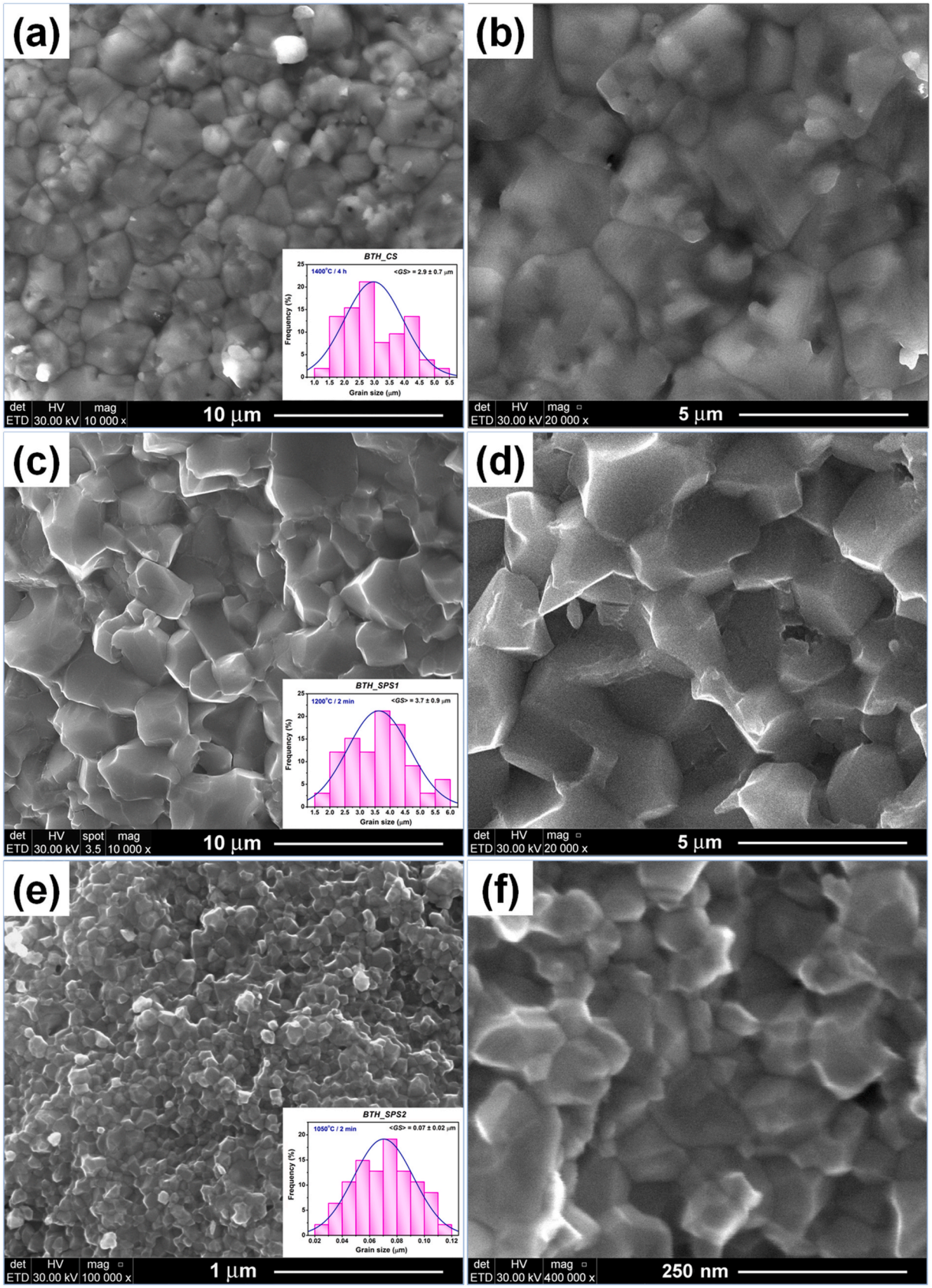

Fig. 6. FE-SEM images of different magnifications: (a), (c), (e) images of lower magnification and (b), (d), (h) images of higher magnification, showing the microstructural details for the $BaTi_{0.90}Hf_{0.10}O_3$ ceramics consolidated by various sintering strategies: (a), (b) conventional sintering at 1400 °C/4 h (sample *BTH_CS*); (c), (d) spark plasma sintering at 1200 °C/2 min (sample *BTH_SPS1*) and (e), (f) spark plasma sintering at 1050 °C/2 min (sample *BTH_SPS2*); the insets in the bottom-right corners of Fig. 6(a)–(c) and (e) display the histograms indicating the grain size distributions.

the experiment for the *BTH_SPS2* ceramic was determined. Taking into consideration these results, we can conclude that the structural results are in a good agreement with the qualitative estimations resulted from Landau theory-based calculations (Fig. 2), which show how the phase composition may change according to the random internal stress fields and reducing *GS*. These structural and microstructural differences are expected to provide variable functional properties of the analyzed ceramics.

4.2. Low-field dielectric properties

4.2.1. Temperature-dependent dielectric properties

The low-field dielectric study $BaTi_{0.90}Hf_{0.10}O_3$ ceramics consolidated by the three sintering strategies allows to trace the evolution of the dielectric response across the ferroelectric–paraelectric transition and to identify features associated with domain dynamics, phase transitions, and relaxation mechanisms, highlighting the role of grain size, morphology and densification in shaping the dielectric response. The temperature-dependent dielectric response was analyzed over a broad frequency range (10^2 Hz–10^6 Hz) in terms of the real part of the permittivity (ε') (Fig. 7(a)–(c), (d)) and dielectric losses (tan δ) (Fig. 7 (b)–(d), (f)).

The coexistence of various structural modifications in a broadened temperature range as a result of the proximity and diffuseness of the ferroelectric-to-paraelectric phase transition has been reported for $BaTi_{0.90}Hf_{0.10}O_3$ ceramics obtained by the classical solid-state reaction method [32,38,39]. For the present BTH samples, a broad prominent peak observed around 340 K in the temperature dependence of the real part of the dielectric permittivity (ε') corresponds to the ferroelectric–paraelectric phase transition, irrespective to the consolidation method. The wide permittivity maxima comprise the room temperature range, where the structural data indicated phase coexistence for all the samples, with variable amounts of the O, T, R and C polymorphs. The transition is sharper and is characterised by the highest permittivity maximum for *BTH_SPS1* (~6510 at 100 Hz), which indicates that a well-defined long-range ferroelectric order is retained. The position of the permittivity maximum remains constant across the investigated frequencies, with only a subtle frequency dispersion of $\varepsilon'(T)$ just below the transition (inset of Fig. 7(a)). Thus, while the Curie temperature (T_C) is unchanged, the permittivity values below T_C show increasing separation with decreasing frequency. This behaviour points to the emergence of frequency-dependent polarization dynamics, typically associated to the onset of local polar instabilities. Such a mild dispersion, in the absence of a frequency shift of the T_C towards higher temperatures, is characteristic of a material exhibiting incipient relaxor crossover regime.

The incorporation of Hf^{4+} ions on Ti sites into [TiO_6] octahedra are triggering local polarization fluctuations below T_C and contribute to frequency-dependent dielectric response. However, long-range ferroelectric domains still dominate the overall polarization mechanism. Above T_C, the permittivity curves merge and follow a nearly frequency-independent linear decrease, characteristic of a paraelectric phase. The dielectric losses (Fig. 7(b)) remain low and stable, with tan δ values typically below 0.13 at 1 MHz, indicating excellent dielectric performance and minimal energy dissipation associated with both conduction and relaxation processes across the entire investigated temperature range. The slightly higher losses at elevated frequencies indicate modest frequency dispersion due to the presence of a weak dipolar relaxation process associated with intrinsic lattice dynamics. The rise in losses observed above T_C reflects the increasing contribution of thermally activated charge carriers, which become more mobile at elevated temperatures and are able to follow low-frequency electric fields. This leads to enhanced energy dissipation at lower frequencies. The onset of conduction-related mechanisms, such as interfacial polarization and Maxwell – Wagner-type relaxation occurs at grain boundaries below ~10^3 Hz. These effects are largely suppressed at higher frequencies, where the dielectric response remains dominated by intrinsic polarization processes and tan $\delta = 0.07$ at 1 MHz.

Compared to the almost fully densified *BTH_SPS1* sample, the conventionally sintered $BaTi_{0.90}Hf_{0.10}O_3$ specimen (*BTH_CS*) exhibits a ferroelectric-paraelectric phase transition with a significantly lower permittivity maximum (~3352 at 10^2 Hz), located at $T_C \approx 340$ K (Fig. 7 (c)). Although the *GS* in both samples is comparable, the *BTH_CS* sample has ~6 % porosity, which explains the reduction in permittivity. The phase transition appears broader and more diffuse, with $\varepsilon'(T)$ curves exhibiting frequency dispersion on both sides of T_C. The permittivity decreases with increasing frequency, from ~3352 at 10^2 Hz down to ~2357 at 10^6 Hz, yet the temperature of the dielectric maximum remains unchanged, indicating that the material does not exhibit relaxor behaviour (inset of Fig. 3(c)). These features are instead consistent with a more diffuse phase transition, likely enhanced by microstructural inhomogeneities and local compositional disorder. The dielectric loss tangent (tan δ), presented in Fig. 7(d), remains below 7 % for $T < T_C$ and is slightly lower than that of the *BTH_SPS1* in this regime. However, tan δ increases above T_C, showing stronger frequency dependence, particularly at low frequency values. This behaviour is attributed to the less compact microstructure and lower grain size involving a more extended network of grain/pore boundaries, which facilitate interfacial polarization processes, such as Maxwell–Wagner-type relaxation. The onset of thermally activated conduction mechanisms further contributes to dielectric dissipation, leading to a steep increase in tan δ values, reaching up to 0.8 at 10^2 Hz.

As illustrated in Fig. 7(e), $\varepsilon'(T)$ dependence of the nanocrystalline ceramic specimen consolidated by SPS at lower temperature (*BTH_SPS2*) exhibits a broad and asymmetric peak, significantly lower in magnitude than those of the above-discussed microstructured ceramics, with a maximum ε' of ~2088 at 10^2 Hz. The transition range is the broadest in this sample and the maximum permittivity range is closest to the room temperature, which explains the important amount of the C polymorph found by the XRD analyses. A defining characteristic of this sample is the frequency dependence of the transition temperature, which shifts from ~330 K at low frequencies (10^2 Hz) to ~340 K at high frequencies (10^6 Hz), as shown in the inset of Fig. 7(e). This frequency dispersion of T_C is a well-established signature of relaxor behaviour, indicative of a dynamic response governed by the freezing of polar nanoregions (PNRs), unlike the sharp phase transition typical for classical ferroelectrics. This dielectric relaxation is strongly linked to the nanostructure. The nanosized grains induce a high concentration of grain boundaries and local structural heterogeneities due to the inhomogeneous strain-stress local fields, which disrupt long-range ferroelectric order and facilitate the development of short-range, dynamic polar correlations. The resulting behaviour aligns well with the characteristics of a relaxor ferroelectric, or at minimum, a system undergoing a relaxor crossover.

Fig. 7(f) shows moderate and well-controlled dielectric losses across the entire temperature range. The values of tan δ range from ~0.14 at 50 K and 10^6 Hz, and gradually decrease with both decreasing frequency and increasing temperature, reaching values as low as ~0.008 at 460 K and 10^2 Hz. Unlike the coarser samples, no sharp increase in tan δ is observed above T_C, indicating a suppression of conduction-related losses due to the nanostructure of the *BTH_SPS2* specimen. In this case, the gradual and continuous decrease in tan δ with increasing temperature, along with its broad and frequency-dependent profile, further supports the presence of relaxor-type dielectric relaxation mechanisms.

4.2.2. Modified Curie–Weiss analysis at multiple frequencies

In classical ferroelectrics, the permittivity in the paraelectric phase follows the Curie–Weiss law above T_C, as described by Cross [72]. The incorporation of Hf leads to an increase in the diffuseness of the phase transition, as previously suggested by the broadening of the temperature-dependent permittivity peak. The frequency-dispersion of the phase transitions and the degree of diffuseness in Hf-doped $BaTiO_3$ ceramics can be explored using the modified Lorentzian-type

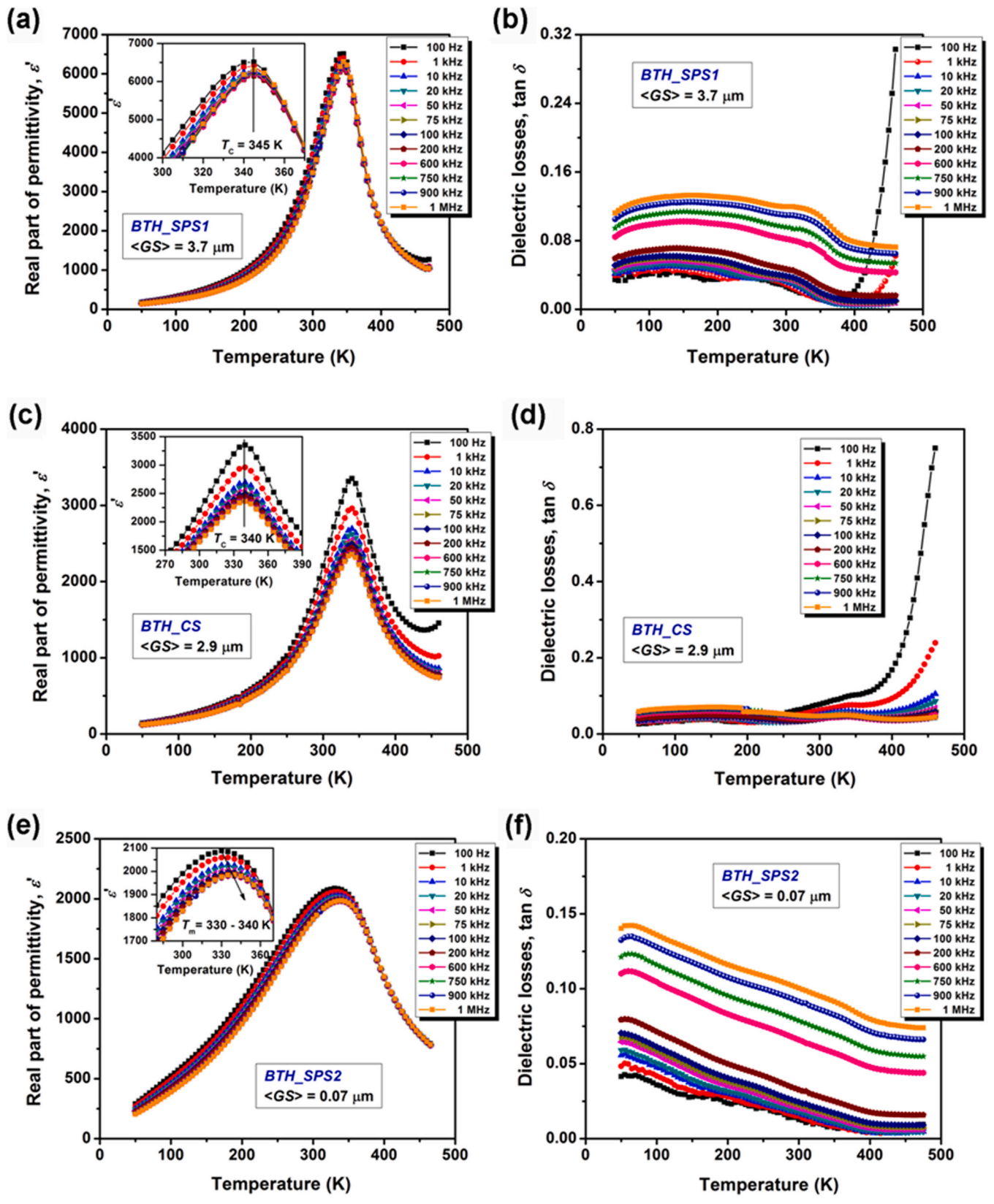

Fig. 7. Temperature dependence of the dielectric response: (a), (c) (e) the real part of permittivity (ε') and (b), (d), (f) the dielectric losses (tan δ) at fixed frequency values ranging between (10^2–10^6) Hz for BTH ceramics consolidated by different strategies: (a), (b) *BTH_SPS1*, (c), (d) *BTH_CS*, and (e), (f)*BTH_SPS2*.

Curie–Weiss equation [73]:

$$\frac{\varepsilon'_m}{\varepsilon} = 1 + \frac{(T - T_C)^\gamma}{2\xi^2}, \quad (5)$$

where: ε'_m is the maximum permittivity at the characteristic Curie temperature T_C, ξ defines the temperature span of the diffuse transition, and γ is the critical exponent characterizing the degree of diffuseness ($\gamma = 1$ for normal ferroelectrics and $\gamma = 2$ for ideal relaxors). By performing this analysis at two representative frequencies of 10^2 Hz and 10^6 Hz, the frequency dependence of the Curie temperature (T_C/T_m), of the maximum permittivity (ε'_m) and of the extent of dispersion are evaluated. The parameters ε'_m, T_C, γ, and ξ resulted from the nonlinear fitting of the experimental data, are summarized in Table S3 of Annex 3, Supplementary Material.

Fig. 8 presents the temperature dependence of both the permittivity analyzed according to the modified Curie – Weiss law and the dielectric losses, at low and at high frequency, respectively.

The variation of the permittivity with temperature, fitted using the modified Curie–Weiss law, is shown in Fig. 8(a) and (b), for frequency values of 10^2 Hz and 10^6 Hz, respectively. The results will be discussed in terms on both the sintering strategy and the measurement frequency.

At 10^2 Hz, the *BTH_SPS1* sample exhibits the highest permittivity value ($\varepsilon'_m = 6538$) and a sharp transition ($T_C = 345$ K) with moderate diffuseness ($\gamma = 1.5$; $\xi = 10.8$ K), indicating a relatively well-preserved long-range ferroelectric order despite doping. *BTH_CS* sample shows a lower permittivity ($\varepsilon'_m = 3459$) and slightly reduced T_C of 340 K, with a narrower transition ($\xi = 7.27$ K) and γ closer to 1 ($\gamma = 1.15$), consistent with a typical ferroelectric behaviour.

The *BTH_SPS2* specimen, which has the finest grain size, stands out by presenting the lowest permittivity ($\varepsilon'_m = 2250$), the lowest T_C (330 K), and a highly diffuse phase transition with $\gamma = 1.76$ and a broad $\xi =$ 38 K. These values clearly suggest a shift from the classical ferroelectric behaviour toward a relaxor-like response influenced by an increased structural disorder and the high density of grain boundaries. From the point of view of the consolidation process, it is clear that fast SPS processing tends to broaden the ferroelectric-paraelectric transitions (as observed when comparing the ξvalues), most likely by creating uncompensated local strain-stress fields, with respect to the equilibrium CS method, which provides as result, sharper permittivity variations in the Curie range. Additionally, the nanostructuring (*BTH_SPS2* sample)

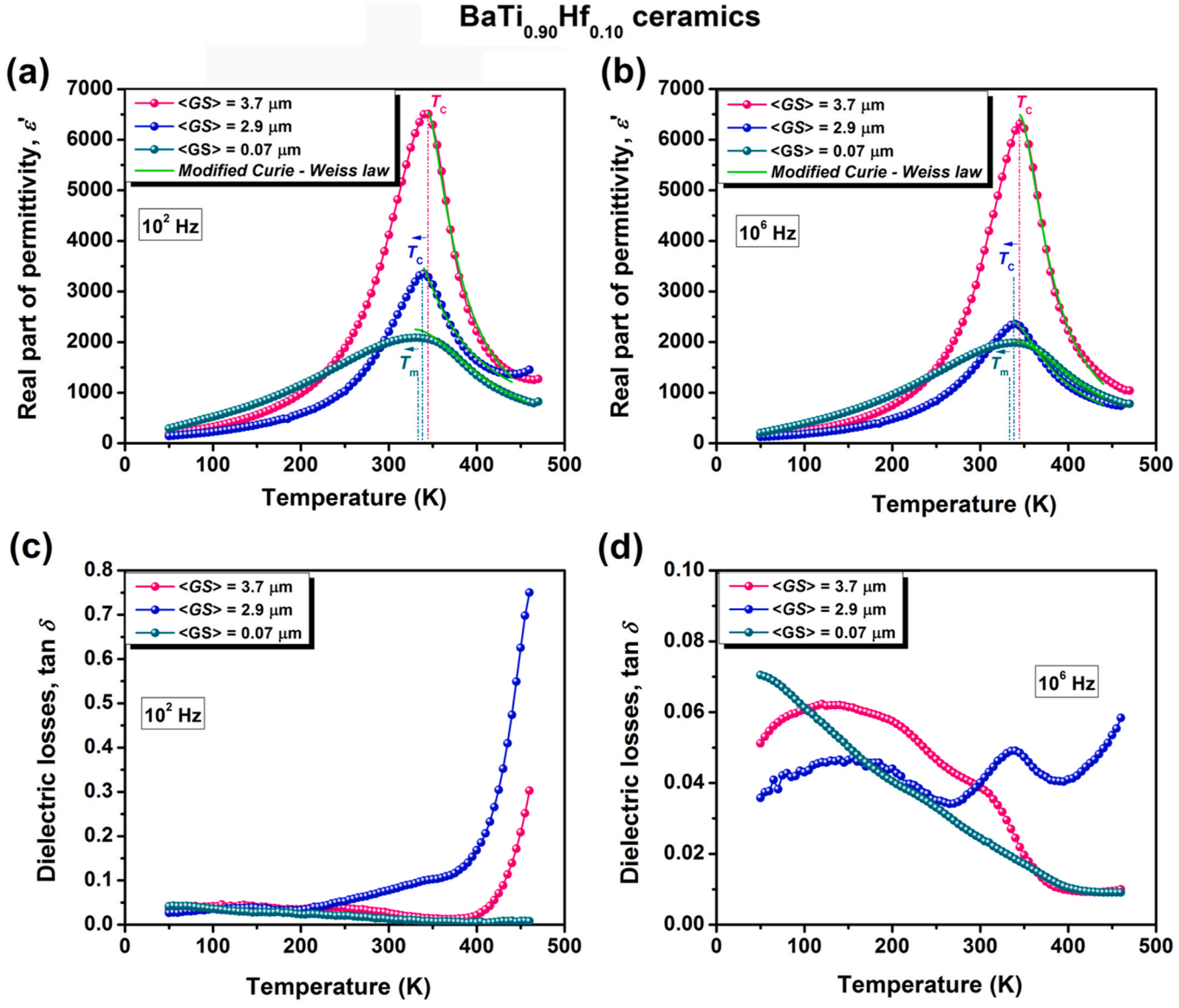

Fig. 8. (a), (b) Temperature dependence of the permittivity, $\varepsilon'(T)$ and analysis according to the modified Curie – Weiss law and (c), (d) temperature dependence of the dielectric losses, tan $\delta(T)$ at fixed frequency values of: (a), (c) 10^2 Hz and (b), (d) 10^6 Hz for BTH ceramics consolidated by different strategies.

enhances the flattening and broadening of the permittivity *vs.* temperature maximum by the presence of a large number of grain boundaries, as already mentioned. At 10^6 Hz, all samples exhibit a reduction in ε'_m due to the limited ability of dipolar entities to follow the high-frequency field. This effect is most pronounced in *BTH_CS* ceramic (ε'_m drops from 3459 to 2391 with ~31 %) and *BTH_SPS_2* (from 2250 to 2010 with ~10.7 %), while for *BTH_SPS_1* the reduction is only of 0.7 % (from 6538 to 6490), suggesting better dielectric stability with frequency. Moreover, both γ and ξ increase with increasing frequency in all samples, which reflects enhanced polarization dispersion.

The Curie temperature remains unchanged for the coarse *BTH_SPS1* and *BTH_CS* ceramics. A slight frequency increase of T_C results for *BTH_SPS2* that shifts from 330 K at 10^2 Hz to 340 K at 10^6 Hz. The observed shift in the nanocrystalline ceramic is specific to the systems with relaxor-like dynamics, where polar nanoregions respond differently depending on the frequency. At low frequencies, slower dipolar entities can contribute to the dielectric response, resulting in a lower apparent T_C. At high frequencies, only faster polar fluctuations can follow the field, and the permittivity maximum slightly shifts to higher temperatures. This frequency-dependent T_C, coupled with the increased broadening of the transition and the reduced permittivity, consolidate the idea that the *BTH_SPS2* specimen exhibits characteristics closer to a relaxor state, driven by the enhanced structural disorder and the high density of grain boundaries associated with the nanostructure.*BTH_SPS1* lies in an intermediate regime, with broadened transitions but still relatively high ε'_m and stable T_C.

The dependence of both the Curie temperature (T_C/T_m) and the maximum permittivity (ε'_m) on the average grain size (<*GS*>) at a frequency of 10 kHz is comparatively presented for the ceramics under investigation and for a BTH ceramic with similar composition, prepared by the solid-state-reaction method by Tian et al. [36] and measured in similar conditions (Fig. S2 of Annex 3, Supplementary Material).

The corresponding variation of loss tangent (tan δ) with temperature increase is displayed in Fig. 8(c) and (d). For both the coarse-grained *BTH_SPS1* and, especially, *BTH_CS* ceramics, the dielectric losses show, at low frequency, a pronounced increase near the transition temperature and above T_C, consistent with conduction or relaxation losses in a system with strong polarization dispersion (Fig. 8(c)). An opposite variation was found in the nanocrystalline *BTH_SPS2* sample, where the dielectric losses decrease 5 times (from 0.04 to 0.008) when the temperature increases from 50 to 460 K. This behaviour can be explained in terms of the a.c. conductivity ($\sigma_{a.c.}$), which decreases with increasing temperature over almost the entire frequency range in the nanocrystalline *BTH_SPS2* specimen (Fig. S4(c) of Annex 5, Supplementary Materials). At high frequency tan δ values are lower and decrease with temperature increasing, especially for *BTH_SPS1* and *BTH_SPS2* (Fig. 8(d)).

To complete the perspective on the dielectric behaviour with a more detailed understanding of polarization dynamics and energy dissipation mechanisms, the response of the BTH ceramics to an alternating electric field was investigated across a broad frequency range. The frequency-dependent dielectric properties and the charge transport mechanisms analyses are presented exhaustively in Annex 4 (containing Fig. S3) and Annex 5 (containing Table S4 and Fig. S4), Supplementary Material. The analysis of a.c. conductivity as a function of frequency and temperature enables the distinction between localized charge carrier dynamics (such as hopping conduction) and long-range conduction mechanisms and provides complementary information on how the conduction mechanisms evolve with microstructure and thermal activation.

4.3. Ferroelectric properties and energy storage performance

The local ferroelectric character was observed by piezoresponse force microscopy PFM (Fig. S5 in Annex 6, Supplementary Material). The coarse-grained *BTH_SPS1* and *BTH_CS* ceramics with micron-sized grains display similar extended and continuous domain structures, with broader domain size distributions. They also contain a significant fraction of larger domain sizes which allow the free domain walls propagation to form long-range ferroelectric domains. The nanocrystalline *BTH_SPS2* specimen comprises mostly single-domain grains, together with larger ferroelectric domains extending over several grains, which are usually pinned due to the grain boundary regions entrapped inside these domains, thus hindering the local ferroelectric switching. This particular feature rather would induce a "frozen" polarization, as found earlier in nanocrystalline $BaTiO_3$ ceramics [74], which is likely to affect to an important extent the macroscopic ferroelectric *P*(*E*) switching process.

Fig. 9(a)–(d) shows the macroscopic ferroelectric *P(E)* loops recorded for the investigated $BaTi_{0.90}Hf_{0.10}O_3$ ceramics. It is clear that the different sintering strategies which provided samples with dissimilar structural modifications and microstructures play an important role on the hysteretic response. The polarization-field (*P*(*E*)) dependences, as well as the polarization and coercive field values are in the same range as reported in both ref. [38] for similar compositions with pseudocubic phase at room temperature (without any data concerning their *GS*) and in Ref. [39], where properties of $BaTi_{0.90}Hf_{0.10}O_3$ with R structure at room temperature and *GS* around 3 − 4 μm have been reported. The ceramic *BTH_SPS1* sustained the application of a high field of 50 kV/cm amplitude, which is enough to provide saturation. It presents a stable polarization-field switching response, with symmetrically shaped well-closed hysteresis loop (Fig. 9(a)) and the characteristics: remanent polarization P_r = 5.5 μC/cm^2, coercive field E =3.8 kV/cm, and rectangularity factor (P_r/P_S) relatively small, of ~0.27.

In *BTH_SPS1*, the saturation polarization value is the highest among the investigated samples, due to the superposition of O, T and R symmetries, which provides 26 allowed polarization states for the ferroelectric switching. The polarization values are smaller with respect to ones reported for coarse ceramics prepared by solid state reaction, with close compositions: 15 μC/cm^2 for $BaTi_{0.89}Hf_{0.11}O_3$, but with larger grains [39] and similar to those ones reported for $BaTi_{0.88}Hf_{0.12}O_3$ (P_r = 7 μC/cm^2) [40]. The slim and tilted loop with high values for the saturation polarization can be explained by the presence at room temperature of the ferroelectric O and T polymorphs, while the small value of the rectangular factor can be attributed to the tendency towards the relaxor character induced by the addition of 10 % Hf.

The ceramic *BTH_CS* sample consolidated by conventional sintering presents a large hysteresis loop with smaller polarization P_r = 5.5 μC/cm^2, E_C = 10 kV/cm and P_r/P_S = 0.49, whose switching behaviour is related to the O and R phase superposition, to the 6 % porosity level and also contain a high-field resistive lossy contribution.

The hysteretic response of the dense, nanostructured *BTH_SPS2* ceramic is characterized by a very slim and tilted loop, with small hysteresis area and low non-linearity, with respect to that one of *BTH_SPS1*. The *P*(*E*) loop is still not completely saturated at 50 kV/cm field amplitude, for which the remanent polarization is P_r = 0.55 μC/cm^2, the coercive field of E_C = 2 kV/cm and rectangularity factor P_r/P_S = 0.05. This switching behaviour is the result of the synergic effect related to: (*i*) the presence of non-polar C polymorph together with the polar R one detected at room temperature for this ceramic and (*ii*) the nanometric *GS*, which jointly induce a combination between relaxor-like state with almost zero macroscopic polarization and zero coercivity, generated by the 10 % Hf substitution [28,75] with a frozen-like polarization (impossibility of switching due to the domain walls pinning by the extended number of grain boundaries, *i.e.* infinite coercivity), as found in nanocrystalline $BaTiO_3$ ceramics [69,74,76,77]. Therefore, the loop tilting towards a non-hysteretic polarization-field response determined for the *BTH_SPS2* ceramics can be comprehended by the three combined factors induced by the Hf addition and SPS sintering consolidation: the approaching of ferroelectric-relaxor crossover, the *GS* reduction down to nanoscale and the approaching of the paraelectric state around room temperature, as indicated by the presence of C polymorph.

The energy storage performance has been evaluated from the hysteresis loops by estimating four properties: the stored energy density

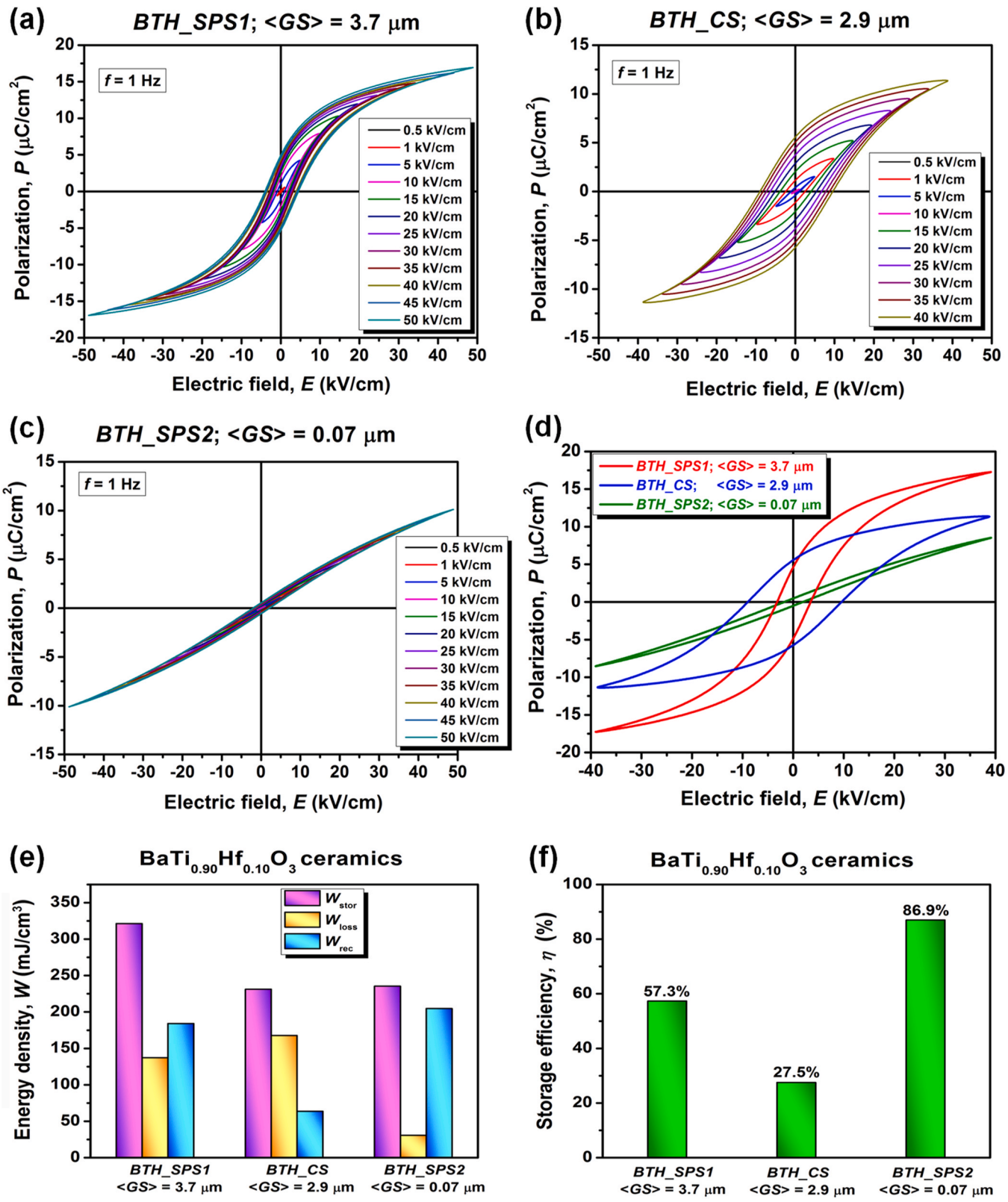

Fig. 9. *P*(*E*) ferroelectric hysteresis loops determined at room temperature (frequency of 1 Hz), under variable electric field amplitudes for the $BaTi_{0.90}Hf_{0.10}O_3$ ceramics produced by various consolidation methods: (a) *BTH_SPS1*; (b) *BTH_CS*; (c) *BTH_SPS2* and (d) comparative hysteresis loops recorded at the maximum applied electric field; energy storage characteristics: (e) energy storage density (W_{stor}), energy loss density (W_{loss}) and recoverable energy density (W_{rec}) and (f) storage efficiency (η), estimated for the applied field $E = 50$ kV/cm.

(W_{stor}), energy loss (W_{loss}), the recoverable energy density (W_{rec}) and the energy storage efficiency (η), according to eq. (6) [78]:

$$W_{stor} = \int_0^{P\ max} EdP;\ W_{rec} = \int_{Pr}^{P\ max} EdP;\ W_{loss} = W_{stor} - W_{rec};\ \eta = \frac{W_{rec}}{W_{rec} + W_{loss}} \quad (6)$$

The influence of grain size, *GS* on these properties is revealed in Fig. 9(e) and (f). Among the BTH investigated samples, it is noticed the advantage of using SPS consolidation in providing higher energy densities and lower energy loss, thus inducing high storage efficiency with respect to the classical sintering sample. The ultrafine nanocrystalline *BTH_SPS2* ceramic has a storage efficiency η of 86.9 %, which is superior to the one reported for fine-grained $Ba_{0.6}Sr_{0.4}TiO_3$ ceramics with almost similar grain size, investigated in the past ($\eta \sim 70$ %) [71]. Both the SP-sintered BTH ceramics have storage performances similar to those ones reported for other $BaTiO_3$-based ceramics [7], as for example in nanostructured BT ceramics with *GS* = 136 nm [79], in $Ba_{0.3}Sr_{0.7}TiO_3$ solid solutions [80], in local compositionally graded relaxor ferroelectric $BaTiO_3$@$SrTiO_3$ with core-shell structure [81], or in $(Ba_{0.70}Ca_{0.30})TiO_3$ ceramics, with a lower efficiency [82], etc.

4.4. Short-range ordering and evolution of phase transitions vs. temperature by Raman spectroscopy investigations

Raman spectroscopy represents a complementary investigation technique, more sensitive than XRD in revealing peculiar local distortions induced by doping and/or by nanostructuring in $BaTiO_3$-based materials. Even if for other homovalently *B*-site substituted barium titanate solid solutions as $Ba(Ti,Zr)O_3$ (BTZ) and $Ba(Ti,Sn)O_3$ (BTS) extensive Raman spectroscopy studies have been performed and many data have been reported in this sense [83–86], the literature regarding structural modifications analyzed by Raman scattering in $Ba(Ti,Hf)O_3$ceramics is scarce [40,52,87,88]. Raman spectra recorded at room temperature for BTH ceramics with various grain sizes determined by dissimilar consolidation strategies are displayed in Fig. 10.

In the low-wavenumber zone (region 1), the main features specific to the ferroelectric $BaTiO_3$ as the sharper peaks assigned to the phonon modes located at 103 cm^{-1} [*E*(TO)], 185 cm^{-1} [$A_1(TO_1)$) + *E*(LO)] and 296 cm^{-1} [B_1, *E*(TO + LO)], but also the broad, asymmetric band located at 230 cm^{-1} [$A_1(TO_2)$], were detected for all the three BTH ceramics. For the microstructured *BTH_SPS1* and *BTH_CS* samples the Raman spectra at room temperature seem quite similar. The presence of the already mentioned sharp peaks, particularly of the "silent" mode [B_1, *E* (TO + LO)] located at 296 cm^{-1}, together with the interference dip at 174 cm^{-1} clearly indicate the long-range polar order, proving that these BTH ceramics are found at room temperature in the ferroelectric state, which sustains the XRD data, as well as the results regarding the low-field dielectric response *vs.* temperature. It is worth to mention that the triple mode (peaks at 113, 137 and 164 cm^{-1}) is specific to the rhombohedral (R) phase [19,89–91]. The interference dip at 124 cm^{-1} is ascribed to the coupling between [A_1(TO)] modes [83] due to the presence in the crystalline lattice of dissimilar BO_6 octahedra determined by the high difference in ionic radius between the substituted Ti^{4+} and substituting Hf^{4+} species. These features were also found in the Raman spectrum of bulk $BaTi_{0.90}Zr_{0.10}O_3$ ceramics, proving the presence of R distortion at room temperature in *B*-site substituted $BaTiO_3$ systems. The small peak located at 185 cm^{-1}, visible a left-side asymmetric feature of the [A_1(TO)] mode is assigned by some authors to the [A_1(TO) + *E*(LO)] phonon mode specific to an orthorhombic (O) local order [89, 92]. All these room-temperature characteristics indicating polar order are also maintained in the nanocrystalline *BTH_SPS2* specimen, but they are less intense due the overall flattening of the Raman spectrum. This can be explained in terms of the appearance of a certain amount of pseudo-cubic phase, rather originated in the stress-induced distortions in the grain-boundary regions than in the proximity of the ferroelectric-to-paraelectric phase transition.

In the high-wavenumber zone, denoted as region 2 (Fig. 10), the

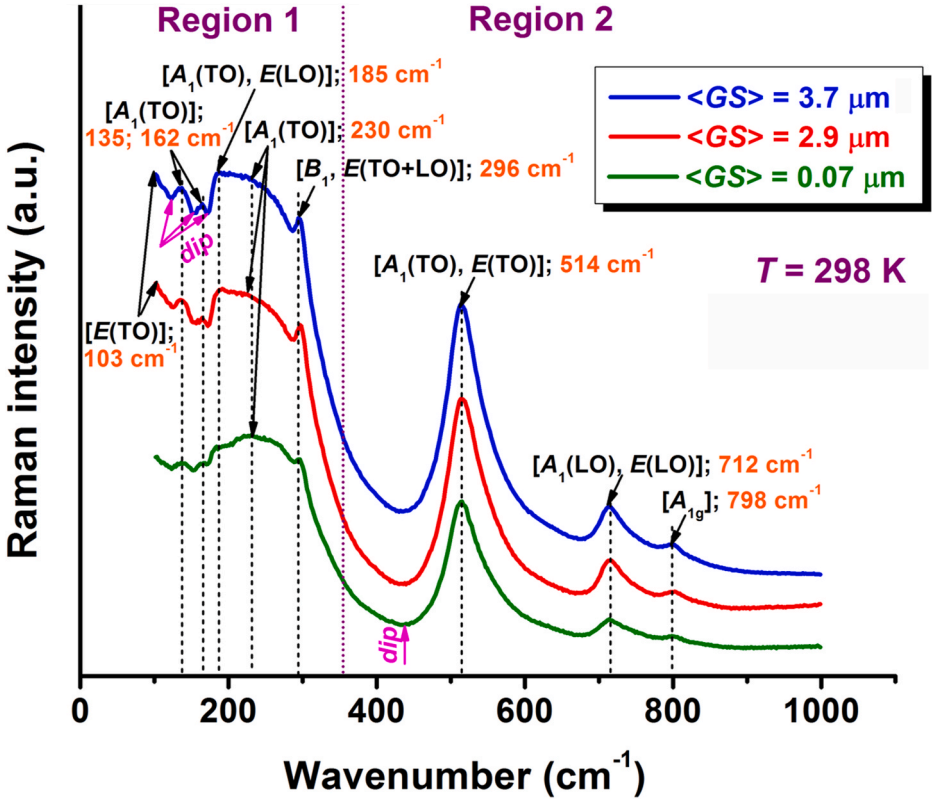

Fig. 10. Raman spectra collected at room temperature for $BaTi_{0.90}Hf_{0.10}O_3$ ceramics with various grain sizes.

broad [A_1(TO) + E(TO)] band located at 514 cm^{-1}, together with the [A_1(LO) + E(LO)] band at 712 cm^{-1} (also specific to the polar order) were detected in the Raman spectra of all the BTH ceramics, irrespective of their consolidation method. A supplementary mode [A_{1g}] was noticed at 798 cm^{-1}. Sati et al. have clearly shown that this mode is not related to a structural modification, but it is caused by the structural disorder [87] determined by the solute incorporation in Ti sites, being the signature of the *B*-site doping in perovskite $BaTiO_3$-based systems [19, 93–96].

To assess the temperature-induced structural changes, as well as the diffuseness of the ferroelectric-paraelectric phase transition in the investigated BTH samples, Raman scattering was recorded in the temperature range of (148–473) K, as depicted in Fig. 11(a)–(d).

At temperatures values $T \leq 173$ K typical features (*i.e.* positive peaks at 118, 143, 165 and 490 cm^{-1}, a broad band at ~260 cm^{-1}, along with interferences deep at 121, 152 and 174 cm^{-1}) specific to the R phase are present in the Raman spectrum of the microstructured *BTH_CS* ceramic (Fig. 11(a)). The increase of temperature determines the damping of the

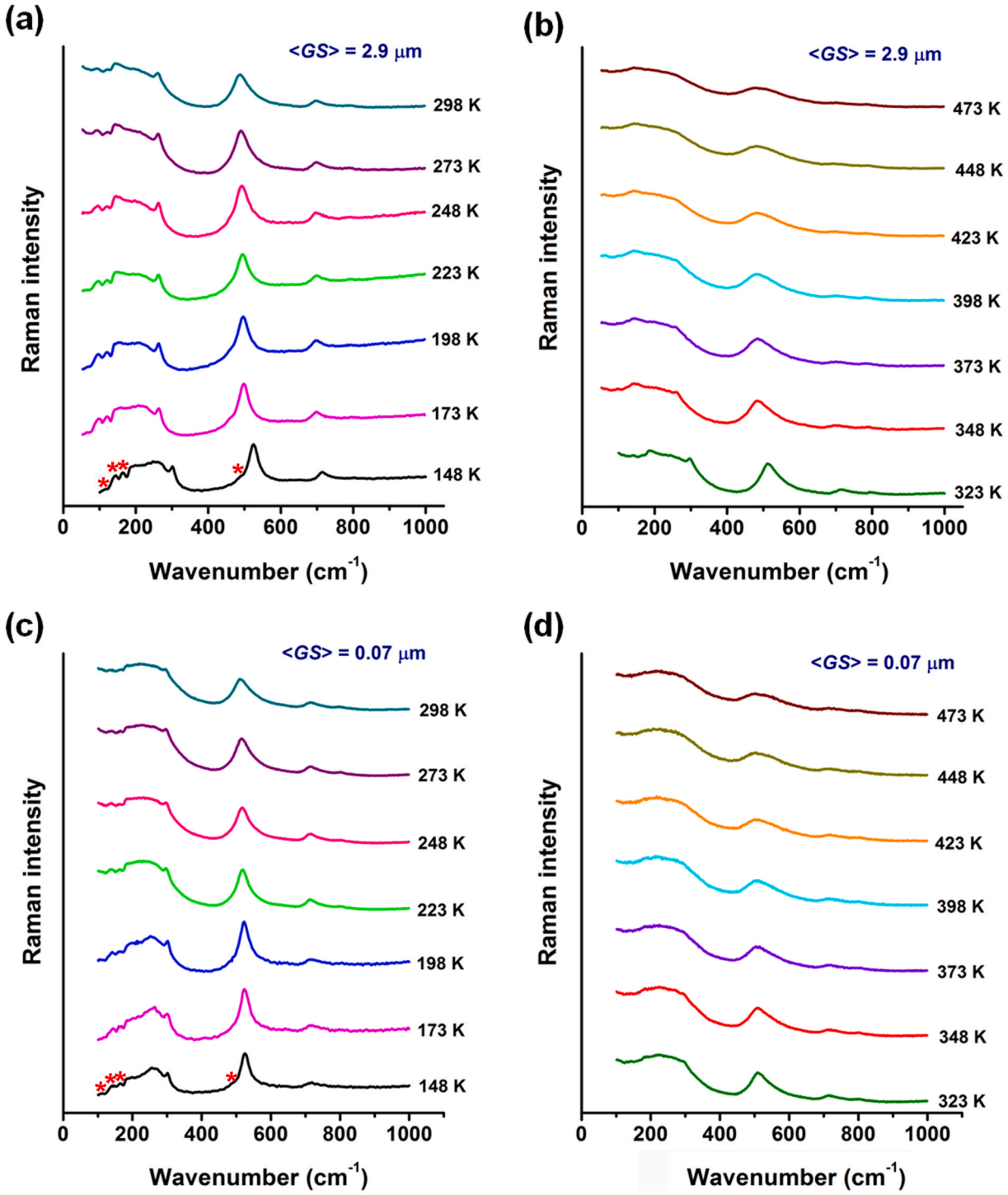

Fig. 11. Temperature dependence of Raman scattering for the: (a), (b) microstructured *BTH_CS* sample (<*GS*> = 2.9 μm) and nanocrystalline *BTH_SPS2* sample (<*GS*> = 0.07 μm) recorded in the temperature range of: (a), (c) (123–298) K and (b), (d) (323–473) K (red asterisk symbols in Fig. 11(a) and (c) indicate the modes corresponding to the R phase).

triple mode, as well as of the of the small mode [E(TO) + A_1(LO)] at 490 cm^{-1}, together with the flattening and downshift of the [A_1(TO)] mode from 262 to 249 cm^{-1}. This occurs concurrently with the slight increase in intensity of both the left- and the right-side neighbouring interferences [A_1(TO$_1$)) + E(LO)] located at ~187 cm^{-1} and [B_1, E(TO + LO)] located at 300 cm^{-1}, indicating the presence of the long-range ferroelectric order in the crystalline lattice [90,91], with a gradual transition from the R toward a polar O symmetry [19]. However, R modification is still maintained at room temperature, proving that Hf-rich regions with R distortion are still present [97]. This is consistent with the XRD data (Table S2 of Annex 2, Supplementary Material), which revealed that at room temperature, a mixture of O and R modifications, with the prevalence of the O-type one exists in *BTH_CS*.

In the temperature range 300–373 K the spectra can be well fitted by the peaks collections corresponding to both O and T phases, suggesting the presence of a mixture of the two polymorphs [29,47,49]. These features were also found in the Raman spectra of microstructured $BaTi_{0.90}Zr_{0.10}O_3$ ceramics derived from Pechini nanopowders, as previously reported [19]. Above 373 K, the gradual disappearance of the "silent" mode and the decrease in intensity of the mode at located at 713 cm^{-1} reveal the gradual change toward a C structure. However, taking into account that, even at 448 K, a trace of the small feature at 187 cm^{-1} persists, it seems that the system evolves not to a typical C phase, but rather to a cubic matrix in which small polar clusters are still present (Fig. 11(b)).

Downscaling grain size in the nanometre range in *BTH_SPS2* determines no significant structural changes in the low temperature range, so that the R modification is detected by its specific modes (Fig. 11(c)). However, unlike the micro-structured sample discussed above, the [A_1(TO)] mode, located at 252 cm^{-1}, is better defined, while its small left-side shoulder, *i.e.* [A_1(TO$_1$)) + E(LO)] interference at 187 cm^{-1} is significantly less pronounced, suggesting that even if the presence of a short-range O distortion cannot be excluded, it is found only in low amount.

At higher temperatures the bands specific to the polar order gradually diminish, indicating an even faster evolution toward a C phase than in the microstructured *BTH_CS* specimen (Fig. 11(d)). Traces of R distortion are still detectable up to room temperature, while the "silent" mode [B_1, E(TO + LO)] is clearly visible up to 348 K. Above this temperature, only small traces of this mode can barely be guessed, this suggesting the presence of small polar clusters which completely vanish above 373 K. These features, together with the broadening of the Raman spectra indicate the occurrence of C structure, specific to the paraelectric state (Fig. 11(d)).

The mentioned trend is also noticed in Fig. 12(a), which depicts the Raman scattering recorded at 473 K for all the three BTH samples, revealing that the grain size decrease toward the nanometre range in *BTH_SPS2* determines the complete disappearance of any polar order. In the coarse-grained *BTH_SPS1* and *BTH_CS* ceramics, the [A_1(TO$_1$)) + E(LO)] interference located at ~188 cm^{-1} is still clearly distinguished, along with residues of the "silent" [B_1, E(TO + LO)] mode (marked by green bullet symbols), barely visible at ~300 cm^{-1} as a small right-side asymmetric features of the broadened [A_1(TO)] band, proving that, for these microstructured samples, a certain polar order persists far above the Curie temperature. This evolution can be explained in terms of a somewhat more rapid shift of the T_C toward lower temperature values, as grain size decreases to the nanometre range, so that, at 473 K, only the nanocrystalline *BTH_SPS2* ceramic exhibits an undoubted C structure, specific to a typical paraelectric phase.

This is also clearly emphasized by the diagram of Fig. 12(b) which presents the temperature dependence of the wavenumber corresponding to the [A_1(TO), E(TO)] mode located at 514 cm^{-1}, revealing temperature ranges where phases of dissimilar symmetries coexist, as also reported for other homovalent $BaTiO_3$-based solid solutions [70,71]. One can observe that, while at room the nanocrystalline *BTH_SPS2* sample exhibits a mixture of R and C phases, for the microstructured *BTH_CS* ceramic a phase domain, where R and O polymorphs coexist was found. These results are in a very good agreement with the room-temperature XRD data presented in Table S2 of Annex 2, Supplementary Material and with the crystalline phase *vs.* temperature evolution derived from Landau-theory based simulations, in which the superposition of dissimilarly-distorted phases in a broad temperature range is typical to the stress-free, coarse ceramic (assigned to *BTH_CS*), while an evolution from R to C symmetry, without the presence of other polymorphs in the transition range, was found for the stressed ultrafine ceramic (assigned to *BTH_CS2*).

5. Conclusions

The lead-free $BaTi_{0.90}Hf_{0.10}O_3$ (BTH) composition was selected for

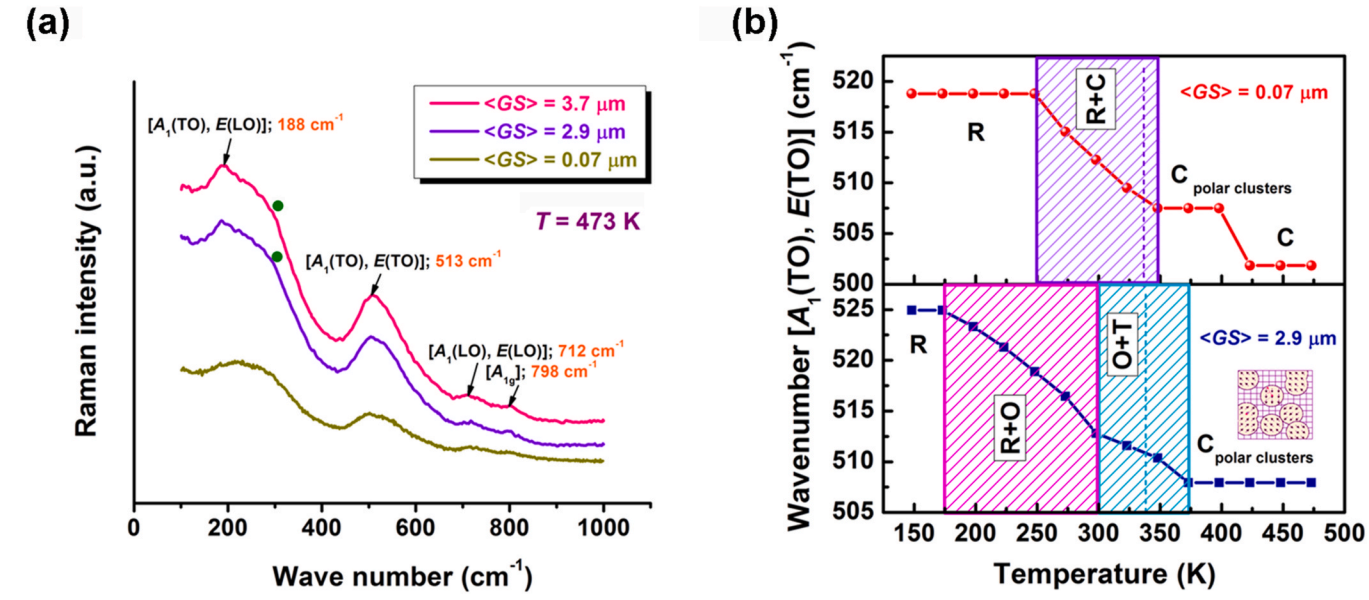

Fig. 12. (a) Raman spectra collected at the temperature of 473 K for $BaTi_{0.90}Hf_{0.10}O_3$ ceramics with various grain sizes (green bullet symbols indicate the residual "silent" mode) and (b) temperature dependence of the wavenumber of [A_1(TO), E(TO)] mode in $BaTi_{0.90}Hf_{0.10}O_3$ with average grain size <*GS*> of 2.9 and 0.07 μm, respectively.

preparing ceramics with various grain sizes, due to the fact that in the proximity of room temperature it determines the overlap of dissimilar structural modifications, providing a pathway to tailor the dielectric and ferroelectric behaviour, as well as the energy storage performance in the resulted perovskite materials. Landau theory-based calculations indicated that for a given composition, additional characteristics derived from the consolidation method (fast spark plasma sintering *vs.* conventional sintering in equilibrium conditions), as grain size reduction to nanoscale (nanostructuring) or the presence of internal stresses may modify the phase composition and the functional properties.

Dense $BaTi_{0.90}Hf_{0.10}O_3$ ceramics of grain sizes ranging between 3.9 and 3.7 μm have been obtained by adopting suitable sintering strategies from nanopowders synthesized by the modified Pechini method. The influence of grain size on the crystalline structure, dielectric properties, ferroelectric behaviour and energy storage performance was investigated by complementary techniques. At room temperature, in all the investigated BTH ceramics, mixtures of dissimilar structural modifications were emphasized by Rietveld refinement of the XRD data and by Raman spectroscopy investigations, sustaining the Landau theory-based calculations. In the microstructured ceramics consolidated by conventional sintering (*BTH_CS*) and by high-temperature spark plasma sintering (*BTH_SPS1*) the O polymorph was identified as major phase, while in the nanocrystalline specimen of similar composition resulted after SPS at lower temperature (*BTH_SPS2*), the R modification prevails. The superiority of SPS relative to conventional sintering lies in the better densification of the materials, as well as in its ability to allow producing nanocrystalline ceramics by careful choice of the sintering parameters. The dielectric response *vs.* temperature shows a single permittivity maximum corresponding to the ferroelectric-to-paraelectric phase transition, whose temperature T_C/T_m slightly decreases and diffuseness increases and as the *GS* decreases. The flattening of the permittivity maximum involving a lower value than in coarse-grained samples, as well as the low dielectric losses (below 3 %) in a large temperature range (from 200 to 460 K) indicate a better thermal stability induced by the *GS* decrease and the consequently increase in the density of grain boundary states in the nanocrystalline specimen. Besides, the decrease of permittivity maximum and its shift to slightly higher temperatures with increasing frequency, together with a certain frequency dispersion of the permittivity values below T_m reveal a ferroelectric-relaxor crossover occurring as a result of nanostructuring. Additionally to the intrinsic dielectric properties, the dielectric response in these ferroelectric ceramics is affected by extrinsic relaxation processes, assigned to a few mechanisms (oxygen vacancy contributions, grain boundary effects, short- and long-range hopping charge carrier mechanisms, etc.). Their contribution on the dielectric permittivity, dielectric losses and ac conductivity has been analyzed in detail. All the ceramics have reasonable low dielectric losses (below 7.5 %) in the frequency range of $10^2 - 10^5$ Hz, below the Curie temperature and an increase of losses at higher temperature (400 − 500 K), due to extrinsic contributions. All the ceramics could sustain the application of ac field with amplitudes as high as 40 − 50 kV/cm while recording the ferroelectric polarization-field responses, thus demonstrating their good dielectric character and the fact that no significant leakage is activated under high ac fields. The *P*(*E*) hysteresis loops show that the interplay between a lower value of the maximum polarization and the much slimmer hysteresis loops lead to a significantly higher energy storage efficiency, of ~87 % in the nanocrystalline specimen (*BTH_SPS2*), with respect to the coarse-grained ceramics, which exhibit, as a function of the consolidation technique, an efficiency of only ~57 % (*BTH_SPS1*) and ~28 %, respectively (*BTH_CS*). Consequently, one can conclude that tuning the grain size <*GS*> in bulk $BaTi_{0.90}Hf_{0.10}O_3$ ceramics leads to changes of the crystal structure of the component phases, providing a powerful tool for tailoring/modifying the functional properties in order to fulfil needs expected for various electronics applications.

Declaration of competing interest

The authors declare that they have no known competing financial interests or personal relationships that could have appeared to influence the work reported in this paper.

Acknowledgement

The authors are grateful to Ministry of Research, Development and innovation through the National Programme "Installations and Strategic Objectives of National Interest" for access to infrastructure. L.P., N.H. and L.M. acknowledge the Romanian grant PN-IV-P1-PCE-2023-1758. R.E.P. acknowledges the financial support from the Core Program of the National Institute of Materials Physics 2023–2026, Project PC2–PN23080202, funded by the Romanian Ministry of Research, Innovation and Digitalization.

Appendix A. Supplementary data

Supplementary data to this article can be found online at https://doi.org/10.1016/j.jmrt.2025.08.195.

References

[1] Lines ME, Glass AM. Principles and applications of ferroelectrics and related materials. Oxford: Clarendon; 1977.
[2] Pan MJ, Randall CA. A brief introduction to ceramic capacitors. IEEE Electr Insul Mag 2010;26(3):44–50. https://doi.org/10.1109/MEI.2010.5482787.
[3] Gulwade D. Lead-free ferroelectrics: barium titanate based ceramics: past, present, and future. In: Swain BP, editor. Advances in nanostructured materials. Materials Horizons: from nature to nanomaterials. Singapore: Springer; 2022. https://doi.org/10.1007/978-981-16-8391-6_18.
[4] Haertling GH. Ferroelectric ceramics: history and technology. J Am Ceram Soc 1999;82(4):797–818. https://doi.org/10.1111/j.1151-2916.1999.tb01840.x.
[5] Capurso JS, Bologna AA, Schulze WA. Processing of laminated $BaTiO_3$ structures for stress-sensing applications. J Am Ceram Soc 1995;78(9):2476–80.
[6] Bell JG, Graule T, Stuer M. Barium titanate-based thermistors: past achievements, state of the art, and future perspectives. Appl Phys Rev 2021;8:031318. https://doi.org/10.1063/5.0048697.
[7] Jain A, Wang YG, Shi LN. Recent developments in $BaTiO_3$ based lead-free materials for energy storage applications. J Alloys Compd 2022;928:167066. https://doi.org/10.1016/j.jallcom.2022.167066.
[8] Adediji YB, Adeyinka AM, Yahya DI, Mbelu OV. A review of energy storage applications of lead-free $BaTiO_3$-based dielectric ceramic capacitors. Energy Ecol Environ 2023;8:401–19. https://doi.org/10.1007/s40974-023-00286-5.
[9] Tagantsev K, Sherman VO, Astafiev KF, Setter J Venkatesh N. Ferroelectric materials for microwave tunable applications. J Electroceram 2003;11(1–2):5–66. https://doi.org/10.1023/B:JECR.0000015661.81386.e6.
[10] Vendik OG. Dielectric nonlinearity of the displacive ferroelectrics at UHF. Ferroelectrics 1976;12(1):85–90. https://doi.org/10.1080/00150197608241397.
[11] Cole MW, Nothwang WD, Hubbard C, Ngo E, Ervin M. Low dielectric loss and enhanced tunability of $Ba_{0.6}Sr_{0.4}TiO_3$ based thin films via material compositional design and optimized film processing methods. J Appl Phys 2003;93(11):9218–25. https://doi.org/10.1063/1.1569392.
[12] Agrawal S, Guo R, Agrawal D, Bhalla AS. Tunable BST:MgO dielectric composite by microwave sintering. Ferroelectrics 2004;306(1):155–63. https://doi.org/10.1080/00150190490460803.
[13] Liu W, Ren X. Large piezoelectric effect in Pb-free ceramics. Phys Rev Lett 2009;103:257602. https://doi.org/10.1103/PhysRevLett.103.257602.
[14] Wu H Tao H, Liu Y, Zhang Y, Wu J, Li F, Lyu X, Zhao C, Xiao D, Zhu J, Pennycook SJ. Ultrahigh performance in lead-free piezoceramics utilizing a relaxor slush polar state with multiphase coexistence. J Am Chem Soc 2019;141(35):13987–94. https://doi.org/10.1021/jacs.9b07188.
[15] Shrout TR, Zhang SJ. Lead-free piezoelectric ceramics: alternatives for PZT? J Electroceram 2007;19:113–26. https://doi.org/10.1007/s10832-007-9047-0.
[16] Fu J, Zuo Z. Structural evidence for the polymorphic phase boundary in NKN based perovskites close to the rhombohedral-tetragonal phase coexistence zone. Acta Mater 2020;195:571–8. https://doi.org/10.1016/j.actamat.2020.06.002.
[17] Maglione M, Bohmer R, Loidl A, Hochli UT. Polar relaxation mode in pure and iron doped barium titanate. Phys Rev B 1989;40:11441–4. https://doi.org/10.1103/PhysRevB.40.11441.
[18] Yu Z, Ang C, Guo R, Bhalla AS. Dielectric properties and high tunability of Ba$(Ti_{0.7}Zr_{0.3})O_3$ ceramics under dc electric field. Appl Phys Lett 2002;81(7):1285–7. https://doi.org/10.1063/1.1498496.
[19] Deluca M, Vasilescu CA, Ianculescu AC, Berger DC, Ciomaga CE, Curecheriu LP, Stoleriu L, Gajovic A, Mitoseriu L, Galassi C. Investigation of the composition-dependent properties of $BaTi_{1-x}Zr_xO_3$ ceramics prepared by the modified Pechini method. J Eur Ceram Soc 2012;32(13):3551–66. https://doi.org/10.1016/j.jeurceramsoc.2012.05.007.

[20] Ianculescu A, Mitoşeriu L. Ba(Ti,Zr)O_3 – functional materials: from nanopowders to bulk ceramics. Hauppauge New York, USA: NovaScience Publishers Inc.; 2010.

[21] Curecheriu LP, Ciomaga C, Mitoseriu L. Temperature-dependent tunability in the paraelectric state of $BaTiO_3$-Based solid solutions. Ferroelectrics 2009;391(1):83–90. https://doi.org/10.1080/00150190903001748.

[22] Ciomaga C, Viviani M, Buscaglia MT, Buscaglia V, Mitoseriu L, Stancu A, Nanni P. Preparation and characterisation of the Ba(Zr,Ti)O_3 ceramics with relaxor properties. J Eur Ceram Soc 2007;27(13–15):4061–4. https://doi.org/10.1016/j.jeurceramsoc.2007.02.095.

[23] Shvartsman VV, Dec J, Xu ZK, Banys J, Keburis P, Kleemann W. Crossover from ferroelectric to relaxor behavior in $BaTi_{1-x}Sn_xO_3$ solid solutions. Ph Transit 2008;81:1013–21. https://doi.org/10.1080/01411590802457888.

[24] Wei X, Yao X. Preparation, structure and dielectric property of barium stannate titanate ceramics. Mater Sci Eng B 2007;137(1–3):184–8. https://doi.org/10.1016/j.mseb.2006.11.012.

[25] Wei X, Feng Y, Wan X, Yao X. Dielectric properties of barium stannate titanate ceramics under bias field. Ceram Int 2004;30(7):1401–4. https://doi.org/10.1016/j.ceramint.2003.12.084.

[26] Müller V, Beige H, Abicht HP. Non-debye dielectric dispersion of barium titanate stannate in the relaxor and diffuse phase-transition state. Appl Phys Lett 2004;84(8):1341–3. https://doi.org/10.1063/1.1649820.

[27] Horchidan N, Ianculescu AC, Curecheriu LP, Tudorache F, Musteata V, Stoleriu S, Drăgan N, Crisan D, Tascu S, Mitoseriu L. Preparation and characterization of barium titanate stannate solid solutions. J Alloy Compd 2011;509(14):4731–7. https://doi.org/10.1016/j.jallcom.2011.01.123.

[28] Horchidan N, Ianculescu AC, Vasilescu CA, Deluca M, Musteata V, Ursic H, Frunza R, Malic B, Mitoseriu L. Multiscale study of ferroelectric-relaxor crossover in $BaSn_xTi_{1-x}O_3$ceramics. J Eur Ceram Soc 2014;34(15):3661–74. https://doi.org/10.1016/j.jeurceramsoc.2014.06.005.

[29] Deluca M, Stoleriu L, Curecheriu LP, Horchidan N, Ianculescu AC, Galassi C, Mitoseriu L. High-field dielectric properties and Raman spectroscopic investigation of the ferroelectric-to-relaxor crossover in $BaSn_xTi_{1-x}O_3$ ceramics. J Appl Phys 2012;111(8):084102. https://doi.org/10.1063/1.3703672.

[30] Canu G, Confalonieri G, Deluca M, Curecheriu L, Buscaglia MT, Asandulesa M, Horchidan N, Dapiaggi M, Mitoseriu L, Buscaglia V. Structure-property correlations and origin of relaxor behaviour in $BaCe_xTi_{1-x}O_3$. Acta Mater 2018;152:258–68. https://doi.org/10.1016/j.actamat.2018.04.038.

[31] Payne WH, Tennery VJ. Dielectric and structural investigations of the system $BaTiO_3$-$BaHfO_3$. J Am Ceram Soc 1965;48(8):413–7. https://doi.org/10.1111/j.1151-2916.1965.tb14779.x.

[32] Anwar S, Sagdeo PR, Lalla NP. Crossover from classical to relaxor ferroelectrics in$BaTi_{1-x}Hf_xO_3$ ceramics. J Phys Condens Matter 2006;18(13):3455–68. https://doi.org/10.1088/0953-8984/18/13/013.

[33] Anwar S, Sagdeo PR, Lalla NP. Ferroelectric relaxor behaviour in hafnium doped barium-titanate ceramic. Solid State Commun 2006;138(7):331–6. https://doi.org/10.1016/j.ssc.2006.03.018.

[34] Anwar S, Sagdeo PR, Lalla NP. Study of the relaxor behaviour in $BaTi_{1-x}Hf_xO_3$ ($0.20 \leq x \leq 0.30$) ceramics. Solid State Sci 2007;9(11):1054–60. https://doi.org/10.1016/j.solidstatesciences.2007.07.023.

[35] Anwar S, Sagdeo PR, Lalla NP. Locating the normal to relaxor phase boundary in $Ba(Ti_{1-x}Hf_x)O_3$ ceramics. Mater Res Bull 2008;43(7):1761–9. https://doi.org/10.1016/j.materresbull.2007.07.013.

[36] Tian HY, Wang Y, Miao J, Chan HLW, Choy CL. Preparation and characterization of hafnium doped barium titanate ceramics. J Alloy Compd 2007;431(1–2):197–202. https://doi.org/10.1016/j.jallcom.2006.05.037.

[37] Garbarz-Glos B, Bak W, Molak A, Kalvane A. Microstructure, calorimetric and dielectric investigation of hafnium doped barium titanate ceramics. Ph Transit 2013;86(9):917–25. https://doi.org/10.1080/01411594.2012.745538.

[38] Li J, Zhang D, Qin S, Li T, Wu M, Wang D, Bai Y, Lou X. Large room-temperature electrocaloric effect in lead-free $BaHf_xTi_{1-x}O_3$ ceramics under low electric field. Acta Mater 2016;115:58–67. https://doi.org/10.1016/j.actamat.2016.05.044.

[39] Li M-D, Tang X-G, Zeng S-M, Liu Q-X, Jiang Y-P, Zhang T-F, Li W-H. Large electrocaloric effect in lead-free $Ba(Hf_xTi_{1-x})O_3$ ferroelectric ceramics for clean energy applications. ACS Sustainable Chem Eng 2018;6(7):8920–5. https://doi.org/10.1021/acssuschemeng.8b01277.

[40] Li M-D, Tang X-G, Zeng S-M, Liu Q-X, Jiang Y-P, Zhang T-F, Li W-H. Phase structure analysis and pyroelectric energy harvesting performance of $Ba(Hf_xTi_{1-x})O_3$ ceramics. J Am Ceram Soc 2019;102(6):3623–9. https://doi.org/10.1111/jace.16237.

[41] Kalyani AK, Brajesh K, Senyshyn A, Ranjan R. Orthorhombic-tetragonal phase coexistence and enhanced piezo-response at room temperature in Zr, Sn, and Hf modified $BaTiO_3$. Appl Phys Lett 2014;104:252906. https://doi.org/10.1063/1.4885516.

[42] Novak N, Weyland F, Rossetti Jr GA. Electrocaloric properties and caloric figure of merit in the ferroelectric solid solution $BaZrO_3$–$BaTiO_3$ (BZT). J Eur Ceram Soc 2021;41(2):1280–7. https://doi.org/10.1016/j.jeurceramsoc.2020.10.017.

[43] Wang G, Lu Z, Li Y, Li L, Ji H, Feteira A, Zhou D, Wang D, Zhang S, Reaney IM. Electroceramics for high-energy density capacitors: current status and future perspectives. Chem Rev 2021;121(10):6124–72. https://doi.org/10.1021/acs.chemrev.0c01264.

[44] Zhang L, Zhao M, Yang Y, Li Y, Tang M, Wang D, Wei X, Liu G, Yan Y, Jin L. Achieving ultrahigh energy density and ultrahigh efficiency simultaneously via characteristic regulation of polar nanoregions. Chem Eng J 2023;465:142862. https://doi.org/10.1016/j.cej.2023.142862.

[45] Wang W, Yang Y, Qian J, Shi W, Huang Y, Jing R, Zhang L, Pan Z, Laletin V, Shur V, Zhai J, Jin L. Advancing energy storage properties in barium titanate-based relaxor ferroelectric ceramics through a stagewise optimization strategy. Chem Eng J 2024;488:151043. https://doi.org/10.1016/j.cej.2024.151043.

[46] Tang XG, Chew KH, Chan HLW. Diffuse phase transition and dielectric tunability of $Ba(Zr_yTi_{1-y})O_3$relaxor ferroelectric ceramics. Acta Mater 2004;52(17):5177–83. https://doi.org/10.1016/j.actamat.2004.07.028.

[47] Maiti T, Gu R, Bhalla AS. Structure–property phase diagram of $BaZr_xTi_{1-x}O_3$ system. J Am Ceram Soc 2008;91(6):1769–80. https://doi.org/10.1111/j.1551-2916.2008.02442.x.

[48] Yu Z, Ang C, Guo R, Bhalla AS. Piezoelectric and strain properties of $BaTi_{1-x}Zr_xO_3$ ceramics. J Appl Phys 2002;92(3):1489–93. https://doi.org/10.1063/1.1487435.

[49] Hennings D, Schnell A, Simon G. Diffuse ferroelectric phase transitions in Ba$(Ti_{1-y}Zr_y)O_3$ ceramics. J Am Ceram Soc 1982;65(11):539–44. https://doi.org/10.1111/j.1151-2916.1982.tb10778.x.

[50] Buscaglia V, Buscaglia MT, Canu G. $BaTiO_3$-based ceramics: fundamentals, properties and applications. Encyclopedia of Materials: Technical Ceramics and Glasses 2021;3:311–44. https://doi.org/10.1016/b978-0-12-803581-8.12132-0.

[51] Yin H-M, Xu W-J, Zhou H-W, Zhao X-Y, Huang Y-N. Effects of phase composition and grain size on the piezoelectric properties of HfO_2-doped barium titanate ceramics. J Mater Sci 2019;54(19):12392–400. https://doi.org/10.1007/s10853-019-03726-y.

[52] Elorika P, Anwar Sh, Anwar S. Impact of synthesis-induced disorder on the structural, electrical, and optical properties of $BaTi_{1-x}Hf_xO_3$, $0 \leq x \leq 0.08$. Mater Res Bull 2023;167:112424. https://doi.org/10.1016/j.materresbull.2023.112424.

[53] Acosta M, Novak N, Rojas V, Patel S, Vaish R, Koruza J, Rossetti Jr GA, Rödel J. $BaTiO_3$-based piezoelectrics: fundamentals, current status, and perspectives. Appl Phys Rev 2017;4:041305. https://doi.org/10.1063/1.4990046.

[54] Bell AJ, Cross LE. A phenomenological Gibbs function for $BaTiO_3$ giving correct E-field dependence of all ferroelectric phase changes. Ferroelectrics 1984;59:197–203. https://doi.org/10.1080/00150198408240090.

[55] Bell AJ. Phenomenologically derived electric field-temperature phase diagrams and piezoelectric coefficients for single crystal barium titanate under fields along different axes. J Appl Phys 2001;89:3907–14. https://doi.org/10.1063/1.1352682.

[56] Li YL, Cross LE, Chen LQ. A phenomenological thermodynamic potential for $BaTiO_3$ single crystals. J Appl Phys 2005;98:064101. https://doi.org/10.1063/1.2042528.

[57] Yao Y, Zhou C, Lv D, Wang D, Wu H, Yang Y, Ren X. Large piezoelectricity and dielectric permittivity in $BaTiO_3$ - $xBaSnO_3$ system: the role of phase coexisting. Europhys Lett 2012;98(2):27008. https://doi.org/10.1209/0295-5075/98/27008.

[58] Liu W, Wang J, Ke X, Li S. Large piezoelectric performance of Sn doped $BaTiO_3$ ceramics deviating from quadruple point. J Alloys Compd 2017;712:1–6. https://doi.org/10.1016/j.jallcom.2017.04.013.

[59] Horchidan N, Padurariu L, Ciomaga CE, Curecheriu L, Airimioaei M, Doroftei F, Tufescu F, Mitoseriu L. Room temperature phase superposition as origin of enhanced functional properties in $BaTiO_3$ - based ceramics. J Eur Ceram Soc 2020;40:1258–68. https://doi.org/10.1016/j.jeurceramsoc.2019.11.088.

[60] Damjanovic D. A morphotropic phase boundary system based on polarization rotation and polarization extension. Appl Phys Lett 2010;97:062906. https://doi.org/10.1063/1.3479479.

[61] Lukacs VA, Airimioaei M, Padurariu L, Curecheriu LP, Ciomaga CE, Bencan A, Drazic G, Avakian M, Jones JL, Stoian G, Deluca M, Brunner R, Rotaru A, Mitoseriu L. Phase coexistence and grain size effects on the functional properties of $BaTiO_3$ ceramics. J Eur Ceram Soc 2022;42(5):2230–47. https://doi.org/10.1016/j.jeurceramsoc.2021.12.024.

[62] Padurariu L, Curecheriu LP, Ciomaga CE, Airimioaei M, Horchidan N, Cioclea C, Lukacs VA, Stirbu RS, Mitoseriu L. Modifications of structural, dielectric and ferroelectric properties induced by porosity in $BaTiO_3$ ceramics with phase coexistence. J Alloys Compd 2021;889:161699. https://doi.org/10.1016/j.jallcom.2021.161699.

[63] Pechini MP. Method of preparing lead and alkaline Earth titanates and niobates and coating method using the same for a capacitor. U S Patent No 1967;3:330–697.

[64] Li B, Wang X, Cai M, Hao L, Li L. Densification of uniformly small-grained $BaTiO_3$ using spark-plasma-sintering. Mater Chem Phys 2003;82(1):173–80. https://doi.org/10.1016/S0254-0584(03)00195-0.

[65] Li B, Wang X, Li L, Zhou H, Liu X, Han X, Zhang Y, Qi X, Deng X. Dielectric properties of fine-grained $BaTiO_3$ prepared by spark-plasma-sintering. Mater Chem Phys 2004;83(1):23–8. https://doi.org/10.1016/j.matchemphys.2003.08.009.

[66] Hoche T, Shen Z, Nygren M, Zhang J, van Aken PA, Heyroth F, Uecker R. Internal strain formed in oxide ceramics upon spark-plasma sintering. Phil Mag 2007;87(29):4555–66. https://doi.org/10.1080/14786430701566036.

[67] Ratzker B, Sokol M. Exploring the capabilities of high-pressure spark plasma sintering (HPSPS): a review of materials processing and properties. Mater Des 2023;233:112238. https://doi.org/10.1016/j.matdes.2023.112238.

[68] Supriya S. Electric field assisted spark plasma sintering of ABO_3 perovskites: crystal structure, dielectric behavior and future challenges. Open Ceram 2024;18:100608. https://doi.org/10.1016/j.oceram.2024.100608.

[69] Zhao Z, Buscaglia V, Viviani M, Buscaglia MT, Mitoşeriu L, Testino A, Nygren M, Johnsson M, Nanni P. Grain-size effects on the ferroelectric behavior of dense nanocrystalline $BaTiO_3$ ceramics. Phys Rev B 2004;70(2):024107. https://doi.org/10.1103/PhysRevB.70.024107.

[70] Pătru RE, Stanciu CA, Surdu VA, Soare EM, Truşcă RD, Vasile BS, Nicoară AI, Trupină L, Pasuk I, Botea M, Horchidan N, Mitoşeriu L, Pintilie L, Pintilie I, Ianculescu AC. Downscaling grain size toward the nanometre range – a key-factor for tuning the crystalline structure, phase transitions, dielectric and ferroelectric behaviour in $Ba_{0.8}Sr_{0.2}TiO_3$ ceramics. Prog Solid State Chem 2024;74:100457. https://doi.org/10.1016/j.progsolidstchem.2024.100457.

[71] Pătru RE, Stanciu CA, Soare EM, Surdu VA, Truşcă RD, Nicoară AI, Vasile BS, Boni G, Amarande L, Horchidan N, Curecheriu LP, Mitoşeriu L, Pintilie L, Pintilie I, Ianculescu AC. Grain size-driven effect on the functional properties in $Ba_{0.6}Sr_{0.4}TiO_3$ ceramics consolidated by spark plasma sintering. J Eur Ceram Soc 2023;43:3250–65. https://doi.org/10.1016/j.jeurceramsoc.2023.02.013.

[72] Cross LE. Relaxor ferroelectrics: an overview. Ferroelectrics 1994;151(1):305–20. https://doi.org/10.1080/00150199408244755.

[73] Uchino K, Nomura S. Critical exponents of the dielectric constants in diffused-phase-transition crystals. Ferroelectrics 1982;44:55–61. https://doi.org/10.1080/00150198208260644.

[74] Buscaglia MT, Viviani M, Buscaglia V, Mitoşeriu L, Testino A, Nanni P, Zhao Z, Nygren M, Harnagea C, Piazza D, Galassi C. High dielectric constant and frozen macroscopic polarization in dense nanocrystalline $BaTiO_3$ ceramics. Phys Rev B 2006;73(6):064114. https://doi.org/10.1103/PhysRevB.73.064114.

[75] Simon A, Ravez J, Maglione M. The crossover from a ferroelectric to a relaxor state in lead-free solid solutions. J Phys Condens Matter 2004;16(6):963–70. https://doi.org/10.1088/0953-8984/16/6/023.

[76] Buscaglia V, Buscaglia MT, Viviani M, Mitoseriu L, Nanni P, Trefiletti V, Piaggio P, Gregora I, Ostapchuk T, Pokorný J, Petzelt J. Grain size and grain boundary-related effects on the properties of nanocrystalline barium titanate ceramics. J Eur Ceram Soc 2006;26(14):2889–98. https://doi.org/10.1016/j.jeurceramsoc.2006.02.005.

[77] Buscaglia MT, Buscaglia V, Viviani M, Petzelt J, Savinov M, Mitoşeriu L, Testino A, Nanni P, Harnagea C, Zhao Z, Nygren M. Ferroelectric properties of dense nanocrystalline $BaTiO_3$ ceramics. Nanotechnology 2004;15(9):1113–7. https://doi.org/10.1088/0957-4484/15/9/001.

[78] Kröll E, Devecioglu L, Salak AN, Piotrowsky L, Shvartsman VV, Lupascu DC. Weakly-coupled barium titanate stannate-based relaxors as energy storage materials. J Am Ceram Soc 2025;108(6):e20413. https://doi.org/10.1111/jace.20413.

[79] Zhu C, Wang X, Zhao Q, Cai Z, Cen Z, Li L. Effects of grain size and temperature on the energy storage and dielectric tunability of non-reducible $BaTiO_3$-based ceramics. J Eur Ceram Soc 2019;39:1142–8. https://doi.org/10.1016/j.jeurceramsoc.2018.11.034.

[80] Wang Y, Shen Z-Y, Li Y-M, Wang Z-M, Luo W-Q, Hong Y. Optimization of energy storage density and efficiency in $Ba_xSr_{1-x}TiO_3$ ($x \leq 0.4$) paraelectric ceramics. Ceram Int 2015;41(6):8252–6. https://doi.org/10.1016/j.ceramint.2015.02.156.

[81] Wu L, Wang X, Gong H, Hao Y, Shen Z, Li L. Core-satellite $BaTiO_3$@$SrTiO_3$ assemblies for a local compositionally graded relaxor ferroelectric capacitor with enhanced energy storage density and high energy efficiency. J Mater Chem C 2015;3(4):750–8. https://doi.org/10.1039/C4TC02291B.

[82] Puli VS, Pradhan DK, Riggs BC, Chrisey DB, Katiyar RS. Investigations on structure, ferroelectric, piezoelectric and energy storage properties of barium calcium titanate (BCT) ceramics. J Alloys Compd 2014;584:369–73. https://doi.org/10.1016/j.jallcom.2013.09.108.

[83] Scalabrin A, Chaves AS, Shim DS, Porto SPS. Temperature dependence of the A_1 and E optical phonons in $BaTiO_3$. Phys Stat Sol (b) 1977;79:731–42. https://doi.org/10.1002/pssb.2220790240.

[84] Chaves A, Katiyar RS, Porto SPS. Coupled modes with A_1 symmetry in tetragonal $BaTiO_3$. Phys Rev B 1974;10(8):3522–33. https://doi.org/10.1103/PhysRevB.10.3522.

[85] DiDomenico M, Wemple SH, Porto SPS, Bauman RP. Raman spectrum of single-domain $BaTiO_3$. Phys Rev 1968;174:522–30. https://doi.org/10.1103/PhysRev.174.522.

[86] Jiang Y-J, Zeng L-Z, Wang R-P. Fundamental and second-order Raman Spectra of $BaTiO_3$. J Raman Spectrosc 1996;27:31–4. https://doi.org/10.1002/(SICI)1097-4555(199601)27:1<31::AID-JRS920>3.0.CO;2-K.

[87] Sati A, Mishra V, Kumar A, Warshi MK, Sagdeo A, Kumar R, Sagdeo PR. Effect of structural disorder on the electronic and phononic properties of Hf doped $BaTiO_3$. J Mater Sci Mater Electron 2019;30:9498–506. https://doi.org/10.1007/s10854-019-01281-5.

[88] Rambadey OV, Kumar A, Sati A, Sagdeo PR. Exploring the interrelation between Urbach energy and dielectric constant in Hf-Substituted $BaTiO_3$. ACS Omega 2021;6(47):32231–8. https://doi.org/10.1021/acsomega.1c05057.

[89] Takeuchi T, Capiglia C, Balakrishnan N, Takeda Y, Kageyama H. Preparation of fine-grained $BaTiO_3$ ceramics by spark plasma sintering. J Mater Res 2002;17:575–81. https://doi.org/10.1557/JMR.2002.0081.

[90] Farhi R, El Marssi M, Simon A, Ravez J. A Raman and dielectric study of ferroelectric $Ba(Ti_{1-x}Zr_x)O_3$ ceramics. Eur Phys J B 1999;9(4):599–604. https://doi.org/10.1007/s100510050803.

[91] Miao S, Pokorný J, Pasha UM, Thakur OP, Sinclair DC, Reaney IM. Polar order and diffuse scatter in $Ba(Ti_{1-x}Zr_x)O_3$ ceramics. J Appl Phys 2009;106(11):114111. https://doi.org/10.1063/1.3253735.

[92] Frey MH, Payne DA. Grain-size effect on structure and phase transformations for barium titanate. Phys Rev B 1996;54:3158–68. https://doi.org/10.1103/PhysRevB.54.3158.

[93] Pokorný J, Pasha UM, Ben L, Thakur OP, Sinclair DC, Reaney IM. Use of Raman spectroscopy to determine the site occupancy of dopants in $BaTiO_3$. J App Phys 2011;109:114110. https://doi.org/10.1063/1.3592192.

[94] Veerapandiyan KV, Khosravi SH, Canu G, Feteira A, Buscaglia V, Reichmann K, Deluca M. B-site vacancy induced Raman scattering in $BaTiO_3$-based ferroelectric ceramics. J Eur Ceram Soc 2020;40:4684–8. https://doi.org/10.1016/j.jeurceramsoc.2020.05.051.

[95] Binhayeeniyi N, Sukvisut P, Thanachayanont C, Muensit S. Physical and electromechanical properties of barium zirconium titanate synthesized at low-sintering temperature. Mater Lett 2010;64:305–8. https://doi.org/10.1016/j.matlet.2009.10.069.

[96] Jiang X, Hao H, Yang Y, Zhou E, Zhang S, Wei P, Cao M, Yao Z, Liu H. Structure and enhanced dielectric temperature stability of $BaTiO_3$-based ceramics by Ca ion B site-doping. J Mater 2020;7(2):295–301. https://doi.org/10.1016/j.jmat.2020.09.001.

[97] Kreisel J, Bouvier P, Maglione M, Dkhil B, Simon A. High-pressure Raman investigation of the Pb-free relaxor $BaTi_{0.65}Zr_{0.35}O_3$. Phys Rev B 2004;69(9):092104. https://doi.org/10.1103/PhysRevB.69.092104.